Type-II interband quantum dot photodetectors

OSCAR GUSTAFSSON

Integrated Devices and Circuits
School of Information and Communication Technology
KTH Royal Institute of Technology

A dissertation submitted to KTH Royal Institute of Technology, Stockholm, Sweden, in partial fulfillment of the requirements for the degree of Teknologie Doktor (Doctor of Philosophy). The public defense will take place on June 14, 2013, 10:00 a.m. in Room D, KTH-Forum, Isafjordsgatan 39, Kista, Sweden.

Cover picture: An edited photograph of a quantum dot photodetector chip from this work mounted on a ceramic carrier.

Abstract

Photon detectors based on single-crystalline materials are of great interest for high performance imaging applications due to their low noise and fast response. The major detector materials for sensing in the long-wavelength infrared (LWIR) band (8-14 µm) are currently HgCdTe (MCT) and AlGaAs/GaAs quantum wells (QW) used in intraband-based quantum-well infrared photodetectors (QWIPs). These either suffer from compositional variations that are detrimental to the system performance as in the case of MCT, or, have an efficient dark current generation mechanism that limits the operating temperature as for QWIPs. The need for increased on-wafer uniformity and elevated operating temperatures has resulted in the development of various alternative approaches, such as type-II strained-layer superlattice detectors (SLSs) and intraband quantum-dot infrared photodetectors (QDIPs).

In this work, we mainly explore two self-assembled quantum-dot (QD) materials for use as the absorber material in photon detectors for the LWIR, with the aim to develop low-dark current devices that can allow for high operating temperatures and high manufacturability. The detection mechanism is here based on type-II interband transitions from bound hole states in the QDs to continuum states in the matrix material.

Metal-organic vapor-phase epitaxy (MOVPE) was used to fabricate (Al)GaAs(Sb)/InAs and In(Ga)Sb/InAs QD structures for the development of an LWIR active material. A successive analysis of (Al)GaAs(Sb) QDs using absorption spectroscopy shows strong absorption in the range 6-12 µm interpreted to originate in intra-valence band transitions. Moreover, record-long photoluminescence (PL) wavelength up to 12 µm is demonstrated in InSb- and InGaSb QDs.

Mesa-etched single-pixel photodiodes were fabricated in which photoresponse is demonstrated up to 8 µm at 230 K with 10 $In_{0.5}Ga_{0.5}Sb$ QD layers as the active region. The photoresponse is observed to be strongly temperature-dependent which is explained by hole trapping in the QDs. In the current design, the photoresponse is thermally limited at typical LWIR sensor operating temperatures (60-120 K), which is detrimental to the imaging performance. This can potentially be resolved by selecting a matrix material with a smaller barrier for thermionic emission of photo-excited holes. If such an arrangement can be achieved, type-II interband InGaSb QD structures can turn out to be interesting as a high-operating-temperature sensor material for thermal imaging applications.

Table of Contents

Acknowledgements

The work behind this PhD thesis was made possible by a long list of people to whom I would like to express my gratitude.

First and foremost I would like to thank Mattias Hammar whose guidance has been key in this work. His broad knowledge of physics and technology, and encouraging support extend way beyond his departmental duties. I have learned more from him during lunch discussions than in any course. He is simply the best supervisor.

I would like to thank Jan Andersson and Sebastian Lourdudoss for giving me the opportunity to be a graduate student and for sharing their experiences. I have appreciated the mixed environment provided by KTH and Acreo. HMA and EKT housed me during my stay. Both are great places to be a student.

Thank you Bertrand Noharet and Susan Savage for introducing me to the world of optoelectronics when taking me in as a diploma student at Acreo, and later on for their excellent project management. The latter has given me experience beyond a traditional graduate education.

A big thanks goes to Jesper Berggren for teaching me everything about MOVPE. I very much enjoyed our discussions in the lab, not least the ones less technical in nature.

Amir Karim´s cheerful and positive way has enabled many of the achievements mentioned in this thesis. He has been an inspiration. This similarly applies to Qin Wang, whose passion for science and interest in people has led her to guide and support students, including me during my diploma- and PhD thesis work.

Linda Höglund has been a great support in exploring the world of quantum dots, always in good spirits.

I would like to thank the guys in the Photonic Devices Group for providing a relaxed and enjoyable atmosphere: Xingang Yu, Yu Xiang, Thomas Zabel and Carl Reuterskiöld-Hedlund. Thomas is particularly acknowledged for his dissemination of the way of scientific writing.

I have very much appreciated the "fika" meetings with infrared imaging theme. Carl Asplund, Hedda Malm, Henk Martijn and Rickard Marcks von Würtemberg made these pleasant and informative.

I have enjoyed the company of many people in Electrum: Carl Junesand (discussing bad action movies never gets old), Anand Srinivasan, Reza Sanatinia, Sam Vaziri, Yanting Sun, Himanshu Kataria, Henry Radamson, Wondwosen Metaferia, Thomas Aggerstam, Andy Zhang, Maziar Manouchehry Naiini, Mohammadreza Kolahdouz Esfahani, Reza Gandhi, Valur Gudmundsson, Eugenio Dentoni Litta, Luigia Lanni, Susanne Almqvist, Sirpa Persson, Fredrik Olsson, Arash Salemi, Audrey Berrier, Mario Siani, Jiantong Li, David Martin, Ali Asadollahi, Anders Hallén, Christopher Ernerheim Jokumsen, Shagufta Naureen, Naeem Shahid, Christian Ridder, Ming-Hong Gau, Ingemar Petermann, Carl-Mikael Zetterling, Stephane Junique, Mikael Östling, Jan Borglind, Sergiy Khartsev, Andrea Pinos, Teresita Qvarnström, Gunnar Malm, Terrence Burks, Reza Nikpars, Jonas Weissenrieder, Michael Tymczenko, Staffan Hellström, Mats Göthelid, Magnus Hårdensson Berntsen, Reyhaneh Soltanmoradi, Anders Eklund, Konstantinos Garidis, Saulius Marcinkevicius, Anders Gamfeldt, Ganesh Jayakumar, Anderson Smith and Katarina Smedfors to name a few.

Thanks also to Sven Valerio and Gunnar Andersson for providing technical assistance and societal insights.

I thank Hans Bergqvist and the rest of the floorball crew for many enjoyable games. Playing with you has been a pleasure.

Last but not least; this would never have been possible without the support from friends and family, most notably, my dear Mikaela. I devote this to you.

Oscar Gustafsson
Stockholm, May 2013

List of papers

Publications included in this thesis

A. **Long-wavelength infrared quantum-dot based interband photodetectors**
O. Gustafsson, J. Berggren, U. Ekenberg, A. Hallén, M. Hammar, L. Höglund, A. Karim, B. Noharet, Q. Wang, S. Almqvist, A. Zhang, S. Junique, J.Y, Andersson, C. Asplund, R. Marcks von Würtemberg, H. Malm and H. Martijn
Infrared Physics & Technology, **54**, 287-291, (2011)

B. **Photoluminescence and photoresponse from InSb/InAs-based quantum dot structures**
O. Gustafsson, A. Karim, J. Berggren, Q. Wang, C. Reuterskiöld-Hedlund, C. Ernerheim-Jokumsen, M. Soldemo, J. Weissenrieder, S. Persson, S. Almqvist, U. Ekenberg, B. Noharet, C. Asplund, M. Göthelid, J.Y. Andersson and M. Hammar
Optics Express, **20**, 21264–21271, (2012)

C. **Long-wavelength infrared photoluminescence from InGaSb/InAs quantum dots**
O. Gustafsson, A. Karim, Q. Wang, J. Berggren, C. Asplund, J.Y. Andersson and M. Hammar
Infrared Physics & Technology, In press, 2013,
http://dx.doi.org/10.1016/j.infrared.2012.12.020

D. **A performance assessment of type-II interband $In_{0.5}Ga_{0.5}Sb$ QD photodetectors**
O. Gustafsson, A. Karim, C. Asplund, Q. Wang, T. Zabel, S. Almqvist, S. Savage, J.Y. Andersson and M. Hammar
Manuscript, submitted to Infrared Physics & Technology, 2013

E. **$GaSb/Ga_{0.51}In_{0.49}P$ self assembled quantum dots grown by MOVPE**
O. Gustafsson, L. Höglund, J. Berggren and M. Hammar
Proceedings from EW-MOVPE XIII, C. 17 273-276, (2009)

Related work not included in the thesis

Journal articles

1. Quantum structure based infrared detector research and development within Acreo's centre of excellence IMAGIC
J.Y. Andersson, L. Höglund, B. Noharet, Q. Wang, P. Ericsson, S. Wissmar, C. Asplund, H. Malm, H. Martijn, M. Hammar, O. Gustafsson, S. Hellström, H. Radamson and P.O. Holtz
Infrared Physics & Technology, **53**, 227-230, (2010)

Conference contributions

2. Development of IR imaging at IRnova
H. Martijn, C. Asplund, H. Malm, S. Smuk, L. Höglund, O. Gustafsson, M. Hammar and S. Hellström
Proc. of SPIE Vol. **7298** 72980E, (2009)

3. Characterization of InSb QDs grown on InAs (100) substrate by MBE and MOVPE
A. Karim, O. Gustafsson, L. Hussain, Q. Wang, B. Noharet, M. Hammar, J. Andersson and J. Song
Proc. of SPIE Vol. **8439** 84391J, (2012)

4. Analysis of surface oxides on narrow bandgap III-V semiconductors leading towards surface leakage free IR photodetectors
Q. Wang, X. Li, A. Zhang, S. Almqvist, A. Karim, B. Noharet, J. Y. Andersson, M. Göthelid, S. Yu, O. Gustafsson, M. Hammar, C. Asplund and E. Göthelid
Proc. of SPIE Vol. **8353** 835311, (2012)

5. Recent developments in type-II superlattice detectors at IRnova AB
H. Malm, R. Marcks von Würtemberg, C. Asplund, H. Martijn, A. Karim, O. Gustafsson, E. Plis and S. Krishna
Proc. of SPIE Vol. **8353** 83530T, (2012)

Patents

Solid-state structure with quantum dots for photodetection of radiation
Inventors: L. Höglund and O. Gustafsson
European Patent Application No. 10169688.8, filed 2010

Acronyms and abbreviations

AFM	atomic force microscopy
FPA	focal plane array
FT-IR	Fourier transform infrared spectroscopy
IR	infrared
I-V	current-voltage
LWIR	long-wavelength infrared
MBE	molecular-beam epitaxy
MCT	mercury cadmium telluride (HgCdTe)
MOVPE	metal-organic vapor-phase epitaxy
MWIR	mid-wavelength infrared
ML	monolayer
NETD	noise-equivalent temperature-difference
PL	photoluminescence
ROIC	read-out circuit
QD	quantum-dot
QDIP	quantum-dot infrared photodetector
QW	quantum-well
QWIP	quantum-well infrared photodetector
SLS	type-II strained layer superlattice
STM	scanning tunneling microscopy
STS	scanning tunneling spectroscopy
TEM	transmission electron microscopy

1 Introduction

1.1 Infrared detection and imaging

Infrared radiation was first discovered by Sir Frederick William Herschel in 1800 when working on designing a telescope for solar observations [1]. His aim was to find an optical filter that would transmit most light while rejecting heat. In his work Herschel used a prism to disperse sunlight and a mercury-in-glass thermometer to detect the radiation. The thermometer is an example of a thermal detector. Detectors of this type absorb light that induces a temperature change, which in turn causes a change in some physical property, e.g. volume, as in the case of Herschel's thermometer. Other examples of thermal detectors include bolometers, which change resistance as a function of temperature [2], pyroelectric detectors which change electrical polarization as a function of temperature [3], and thermocouples, where a temperature dependent electrical potential is created in a junction of dissimilar metals [4]. In contrast, photon detectors absorb radiation by interaction with electrons which are excited to higher energy states. Since this process depends on the electronic energy distribution of the material, photon detectors are wavelength-selective and offer fast response with good noise characteristics [5].

The development of infrared detection has made available a wide range of applications including high-speed data-communication [6], burglar alarms [3], fire detection [7], infrared spectroscopy [8], medical diagnosis of melanoma [9] and industrial process control [10, 11]. In addition, the advancement of photolithography and integrated circuits, with the charge-coupled device (CCD) as a major milestone, has made available infrared sensor arrays for, what are perhaps the most commonly associated applications of infrared detection, night vision and thermal imaging [12]. These have traditionally been used for defense, security and surveillance but civil applications such as automotive safety, fire-fighting and industrial process control, are becoming more common as production costs are reduced [13, 14, 15, 16, 17, 18, 19, 20].

In contrast to the technology used in night vision tubes, which relies on reflected light from the atmosphere, so-called nightglow, or active infrared illumination, thermal imaging can be used to image objects in complete darkness due to their emission of infrared light [21]. This emission is described by Planck's blackbody law [22] presented for different object temperatures in Fig.1. We note that the black-body peak emission at room-

temperature, which is a typical imaged environment, corresponds to an emission wavelength maximum at 10 μm. Since imaging is done at some distance to the object, atmospheric attenuation originating mainly from absorption in the greenhouse gases H_2O and CO_2, needs to be taken into consideration. There are two spectral windows of reasonably high transmission: the mid-wavelength infrared (MWIR) which spans 3-5 μm and the long-wavelength infrared (LWIR) which spans 8-14 μm. Imaging in the LWIR clearly offers a higher photon flux, whereas MWIR imaging provides a better thermal contrast. The strengths and weaknesses of imaging in the respective wave-bands for different conditions were neatly assessed by Miller, who also included the short-wavelength (SWIR) band spanning 1-3 μm [23]. This comparison is presented in Tab.1.
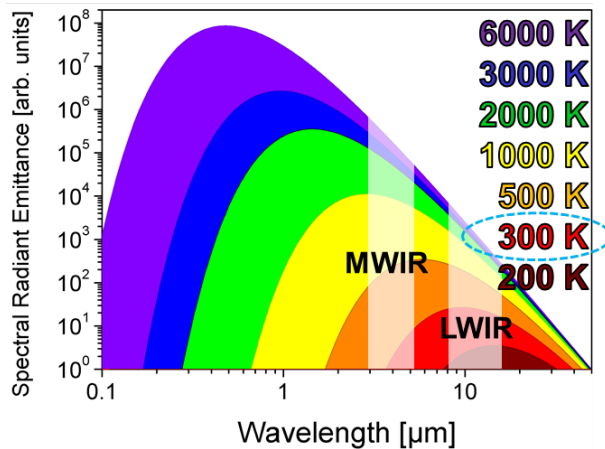
Figure 1. Spectral radiant emittance in arbitrary units presented for black-body objects at different temperatures.

	SWIR	MWIR	LWIR
View through smoke	Better than visible	Better than SWIR	Better than MWIR
High humidity	Better than visible	Best: better than SWIR and LWIR	Moderate
Cold weather night vision	N/A	Moderate	Best
Read painted symbols	Good	Poor	Poor
Night vision in total darkness	Poor – relies on nightglow	Excellent	Excellent
View through fog	Better than visible	Better than SWIR	Better than MWIR

Table 1. Imaging characteristics in three IR spectral regions. Taken from ref. [23].

1.2 Detector technologies

Low-cost infrared imaging technology is at present completely dominated by uncooled bolometers with vanadium oxide as the thermistor material (95 % market share in 2010) [24]. Here, the performance is a trade-off between sensitivity (noise-equivalent temperature difference (NETD)) and response time. This is due to the fact that NETD is proportional to the square-root of the thermal conductance whereas the response time is inversely proportional to the thermal conductance. Thermal time constants in bolometers are typically in the range of milliseconds [25]. This means that the response time at high sensitivity is relatively slow compared to cooled photon detectors which dominate the high performance imaging segment.

Since photon detectors are wavelength-sensitive several different semiconductor materials are used in the IR imaging spectrum. SWIR imaging is typically done using InGaAs/InP [26] whereas InSb bulk material provides cost-effective and uniform arrays in the MWIR spectral range [27]. Constituting the most versatile IR bulk material, the ternary alloy HgCdTe (MCT) bandgap can be tuned between 1.5 eV and 0 eV covering the whole infrared regime [28]. It has been used for LWIR imaging since the 1970s and it has been called "the Ultimate IR Semiconductor" [29]. While it is true that MCT is very versatile due to the alloying of the semiconductor CdTe ($\approx$1.5 eV bandgap at room temperature) and the semimetal HgTe, which share a very similar lattice constant, this also entails a strong sensitivity to growth uniformity. Small variations in the composition across the wafer influence the photoresponse and dark current in detector arrays which cannot be fully compensated for. This can limit the performance and sensitivity in terms of NETD. [24]

An alternative approach are the quantum-well infrared photodetectors (QWIPs) based on inter sub-band transitions. In the LWIR such devices have been widely successful owing much to the maturity of the III-V material platform and high-quality substrates. It is the detector technology of choice in applications that demand highly uniform sensor arrays with pixel operability close to 100% [30]. The quantum efficiency and consequently the integration time are moderate due to the intraband transition, which prohibits absorption of normal incident photons, and the short lifetime of photoexcited carriers [31]. Moreover, the thermionic emission of ground state electrons is efficient leading to dark current generation which imposes strong demands on the cryogenic cooling. An LWIR QWIP is typically operated at approximately 70 K [32].

The need for high quantum efficiency, high operating temperature and good uniformity sensor arrays has spurred an interest to investigate alternative quantum structures in the III-V material platform. Quantum-dot infrared photodetectors (QDIPs) is one example that utilizes intraband transitions in InAs QD/InGaAs/GaAs structures for infrared detection. Here the quasi-three-dimensional confinement of the self-assembled QDs provides an optical matrix element which is non-zero for normal incident photons. This enhances absorption and relaxes the need for grating structures normally used in QWIPs to enable absorption. It furthermore imposes conditions on the electron-phonon interactions, often referred to as the phonon bottleneck effect, which can help to increase the carrier lifetime and consequently the photoconductive gain and the external quantum efficiency [33]. Carrier lifetimes up to 1 ns are predicted which can be compared to the 1-10 ps inter sub-band relaxation time typically measured for quantum wells (QWs) [34]. Nevertheless, recent reports of QDIP detectors show results inferior to QWIPs [35].

During the past few years, detectors based on type-II strained-layer superlattices, hereafter referred to as SLSs, have become the major subject of development efforts in the IR photon detector scientific community. As first proposed by Smith and Mailhiot, these structures contain thin layers of the ternary alloys InAsSb and InGaSb stacked in a periodic structure several micrometers thick [36]. The composition-dependent type-III band alignment between the layers provides tunability of the mini-bands that are formed due to the wave-function overlap between the thin layers. The mini-bands emulate an artificial bulk material with a bandgap that can be tuned in practically the whole IR range. Strained-layer superlattice detectors are predicted to outperform MCT technology due to lower effective masses and longer Auger lifetimes [37, 38, 39, 40]. Presently the epitaxial material quality with mid-gap defect states limits the performance in SLS devices. Recent progress in the epitaxial growth of SLSs shows that the dark current can be lower than in corresponding MCT devices, albeit at a much lower quantum efficiency [41]. However, significant challenges still remain to improve the epitaxial quality in the large amount of strained interfaces which are necessary for achieving the predicted sensitivity with good uniformity.

1.3 About this work

The aim of this thesis is to investigate an alternative approach for infrared photon detection in the LWIR spectrum mediated by type-II transitions in epitaxially grown self-assembled quantum dots (QDs). Figure 2 exemplarily sketches the band structure of an InGaSb QD in an InAs matrix in the growth

direction. The horizontal black line reflects the confined hole state inside the QD valence band. Due to the type-III band alignment electrons are not confined inside the QD. As indicated by the black arrow the absorption occurs through excitation of electrons from bound states in the QD valence band to continuum states in the conduction band of the matrix material surrounding the QD.
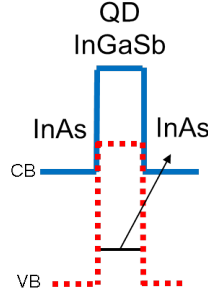

Figure 2. Schematic of the band alignment in the InGaSb QD/InAs heterostructure indicating the type-II optical excitation path through which the absorption occurs.

The spatial separation of carriers entails long lifetimes, which is favorable for extraction of photo-excited carriers and low dark current generation [42, 43]. In addition, the matrix material bandgap is larger than the transition energy for the targeted detection wavelength which can act to suppress Shockley-Read-Hall processes involving defect level- mediated dark current generation. The QDs are, furthermore, highly strained which induces a valence band splitting that can act to reduce Auger generation, similarly as predicted for the case of SLSs. The discrete energy levels resulting from the three-dimensional confinement in a QD have been claimed to inhibit Auger processes due to energy conservation principles, although this is still under debate [44, 45, 46, 47]. The detection mechanism in this detector type does not rely on any quantum mechanical coupling between the QD layers. Strain-distribution is moreover arranged by the self-assembly process and it can potentially relax the requirements on the epitaxy as compared to growth of SLSs.

In this work five QD material systems have been investigated in detail; tensile-strained AlGaAs and GaAsSb QDs, compressively strained InGaSb QDs on InAs substrates and compressively strained InAs and GaSb QDs on GaAs substrates. The principal effort has been focused on the material development of the

active layer in type-II QD photodetectors, with studies of the growth conditions in particular. The material has been grown with metal-organic vapor-phase epitaxy (MOVPE) and has been investigated by a variety of characterization techniques including photoluminescence (PL), absorption measurements, atomic-force microscopy (AFM), transmission electron microscopy (TEM) and scanning tunneling microscopy (STM). Tensile-strained QDs were grown at high densities up to 1×10^{12} cm^{-2} without any optical activity despite of intraband absorption in the MWIR and LWIR spectra [Paper A]. Compressively strained GaSb QDs were grown on GaAs and InGaP with dot densities up to 1×10^{11} cm^2 [Paper E]. Effects of a reduction of Sb interdiffusion and/or segregation were observed in GaSb QD/InGaP structures as compared to GaSb QD/GaAs structures [Paper E]. Compressively strained QDs of InSb were grown and optimized for long PL wavelength, reaching peak PL up to 6.5 µm at 77 K [Paper B]. Inclusion of Ga in the growth of the QDs was used as a mean to extend the wavelength up to the LWIR regime. Reduced strain, due to a smaller lattice mismatch to the substrate, is interpreted to result in the formation of larger QDs with less confinement effects that provides a smaller type-II transition energy corresponding to wavelengths up to 12 µm [Paper C]. Single-pixel type-II QD photodiodes were realized with photoresponse up to 8 µm at 230 K [Paper B, Paper D]. The magnitude of the photocurrent was observed to be strongly temperature-dependent and thermally activated, which is attributed to hole trapping in the QDs. This limits the performance at typical LWIR sensor operating temperatures (60-120 K). Consequently, it necessitates a replacement of InAs with a matrix material that provides a reduced hole barrier for efficient photocurrent collection and improved performance. $InAs_{0.6}Sb_{0.4}$ is suggested as a suitable matrix material.

The here studied type-II QD interband photodetectors fall short in performance compared to state-of-the-art detector technologies such as MCT and QWIP. If the shortcomings of the carrier transport can be resolved, the dark current properties, which differ from MCT and QWIP materials, may enable performance advantages. A potential market segment might then evolve by virtue of 'QWIP-like' performance at increased operating temperatures.

2 Experimental methods

2.1 MOVPE

The word epitaxy refers to a method of placing atoms on top of a substrate material so that the crystallographic arrangement of the deposited material conforms to that of the substrate. It is the basis for fabrication of semiconductor thin films and quantum structures that have been essential in the development of many modern technological advances such as the first compact microwave source (the Gunn diode) [48], the double heterostructure laser [49, 50], the heterojunction bipolar transistor (HBT) [51] and the high-electron-mobility transistor (HEMT) [52]. In particular it allows for industrial scale production of advanced optoelectronic devices such as vertical-cavity surface-emitting lasers (VCSELs).

Normally the substrate is chosen with the same or similar crystal structure and lattice constant as the intended epitaxial layer, but this is not always possible due to inherent difficulties in fabricating bulk crystals of certain materials, such as ternary III/V compounds and GaN [53]. GaN-based thin films, typically used in blue and "white" light-emitting diodes (LEDs), are therefore generally grown on sapphire substrates. Single-crystalline substrates used for epitaxial growth are most commonly fabricated from a melt by the liquid-encapsulation Czochralski (LEC) process, in which cylindrical ingots are pulled from the melt and sliced into discs, called wafers.

In this work, we use the metal-organic vapor-phase epitaxy (MOVPE) technique. Here the source materials are metal-organic compounds and hydrides. The latter are generally gases at standard temperature and pressure (STP) whereas the former typically are in liquid form at STP. Highly purified hydrogen (>99.9999999 % [54]) is used as carrier gas. It is injected into the metal-organic compound containers, called bubblers, where it is saturated with the vapor-phase of the metal-organic compound. The carrier gas transports the source materials towards the heated substrate in the reactor cell. A phenomenological model of the growth is presented in Fig. 3. The sketch illustrates the whole MOVPE process starting with the diffusion of metal-organic compounds towards the substrate. The high temperature in the vicinity of the substrate facilitates a pyrolysis process which thermally decomposes the metal-organic molecules. After that the metal-radical adsorbs on the surface and diffuses towards a surface step on the substrate where the metal reacts chemically with its complementary counterparts forming a

semiconductor crystal. The diffusion length is strongly temperature dependent. At standard growth conditions the incorporation most likely occurs at a step edge which minimizes the surface energy of the semiconductor crystal. It is strongly desired that all organic by-products desorbs from the surface during the process.
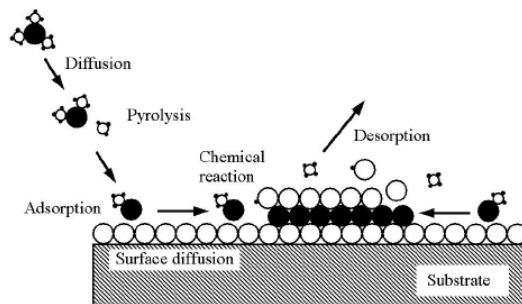

Figure 3. A schematic model of the MOVPE growth process. From Asplund [54] with kind permission from the author.

Growth by MOVPE is often classified in three growth regimes corresponding to the growth rate limiting phonomenon: kinetics, mass-transport and thermodynamics/prereactions.

2.1.1 Growth regimes

Growth of III/V materials using standard sources like trimethylgallium (TMGa), trimethylindium (TMIn), trimethylaluminium (TMAl), arsine (AsH_3) and phosphine (PH_3) is typically done at temperatures below 800 °C. Above this approximate limit pre-reactions in the gas-phase occur which in conjunction with the exothermic nature of the surface reactions can limit the growth rate.

In the conventional growth regime (600-800 °C) surface reactions are relatively fast and the MOVPE process is mass-transport limited with a growth rate that is proportional to the input partial pressure of the group-III species [55]. This is due to the high vapor-pressure property of the conventional group V species (As, P) which acts self-limiting on the incorporation. This is however not true for Sb, used in this thesis for growth of antimonide compounds. Due to the comparably low vapor-pressure of elemental Sb, a precise control near unity ratios of V and III species is required [56]. An additional complication with Sb is that it tends to segregate and intermix with

its surrounding due to its weak bonding properties [57, 58]. This was investigated for GaSb/GaAs and GaSb/InGaP interfaces in Paper E.

Growth of QDs typically requires low growth temperatures (<600 °C) since QD nucleation and dislocation formation are both thermally activated with a barrier that scales with the strain ε as ε^{-4} and ε^{-1} respectively [59]. Low temperature is also needed in order to maintain self-limiting growth, which is controlled by a kinetic barrier at the island edges originating in strain [60]. Unfortunately the low temperature can influence the growth properties in such a way that the growth rate is not anymore mass-transport limited. Instead, surface reactions can be the rate-limiting step making the growth rate strongly dependent on temperature. The exact temperature at which the growth rate becomes surface limited is greatly depends on the material; InAs growth, used extensively in this work, has been reported to be mass-transport limited down to 400 °C [61]. Moreover, low-temperature growth can include incomplete pyrolysis of the precursor molecules and/or incomplete desorption of by-products from the surface. The latter can be observed in e.g. growth of carbon autodoped InAs layers at 350 °C [61] and AlGaAs layers at 500-600 °C. Interestingly, for AlGaAs films, carbon autodoping can in some cases result in tensile strain [54, 62].

2.1.2 Growth modes
The three principal epitaxial growth modes are two-dimensional layer-by-layer growth (Frank-van der Merwe), three-dimensional growth (Volmer-Weber) and Stranski-Krastanov which initially involves two-dimensional growth followed by islanding. The former is of importance for growth of the matrix material in this thesis whereas the latter is the known growth mode for the grown QD systems [63, 64, 65].

2.1.2.1 Layer-by-layer growth
For the case when the adatom diffusion length exceeds the average atomic step terrace width the adatoms will mainly be incorporated at the edges and there will be no nucleation of 2D islands on the terraces. This growth mode is called step-flow [66]. In this mode the reaction rate is fast compared to the adatom arrival deposition rate and the surface coverage is low. At lower temperature ranges when the adatom diffusion length is shorter, growth occurs through 2D islanding. The islands grow in size until they merge.

An example of a surface as defined by homoepitaxy on InAs (001) at 490 °C is given in the ex-situ measured AFM-micrograph in Fig. 4. Here we see an

intermediate mode of step flow with some examples of islanding. We note that this ex-situ measurement may include effects of surface processes during reactor cooling and hence may not truly reflect the surface during growth as observed by Asplund and Bernatz *et al.* for growth interrupts of interior GaAs interfaces [54, 67].
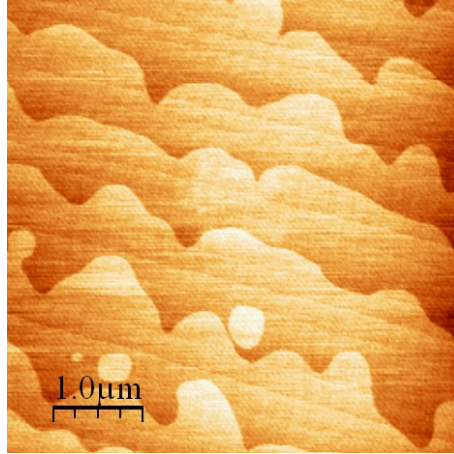

Figure 4. 5x5 μm² AFM micrograph of an InAs (001) surface homoepitaxially grown at 490 °C using TMIn and AsH₃ at V/III input flow ratio 150.

2.1.2.2 Stranski-Krastanov growth

A simple thermodynamical model to describe heteroepitaxial growth modes was devised by Bauer [68]. The model is based on a droplet as sketched in Fig. 5. It considers the surface free energies of the substrate γ_1 and the deposited material γ_2 and their interface energy γ_{12}. For cases when $\gamma_1 > \gamma_2 + \gamma_{12}$ the growth occurs layer-by-layer (Frank-van der Merwe) whereas if $\gamma_1 < \gamma_2 + \gamma_{12}$ growth will occur by islanding (Volmer-Weber) as depicted in Fig. 5.
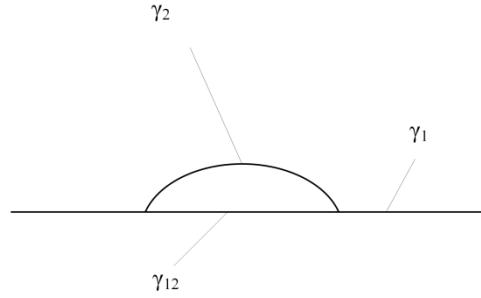
Figure 5. A surface energy model describing heteroepitaxial growth. After Bauer [68].

In the case of lattice-mismatched growth, the lattice mismatch has an effect similar to that of interface energy [60]. Thus, for small values of strain, the growth often results in layer-by-layer growth whereas for large strain, Volmer-Weber islanding can occur with dislocations in the substrate-island interface to accommodate the mismatch. For intermediate strain values, growth can initially occur in 2D followed by 3D islanding, so-called Stranski-Krastanov growth as schematically described in Fig. 6. In this case (Fig. 6 no. 2), the interface energy is such that $\gamma_1 > \gamma_2 + \gamma_{12}$. Due to the buildup of strain-energy when more material is deposited the additional film strain energy term $\mu(t)$ is added to the equation. At the critical thickness t_c, $\gamma_1 < \gamma_2 + \gamma_{12} + \mu(t_c)$ and hence a 2D to 3D growth transition occurs with the film increasing its surface free energy in favor of reducing the strain energy (Fig. 6 no. 3 & 4). At the right conditions elastically strained, coherent islands are formed (Fig. 6 no. 5).
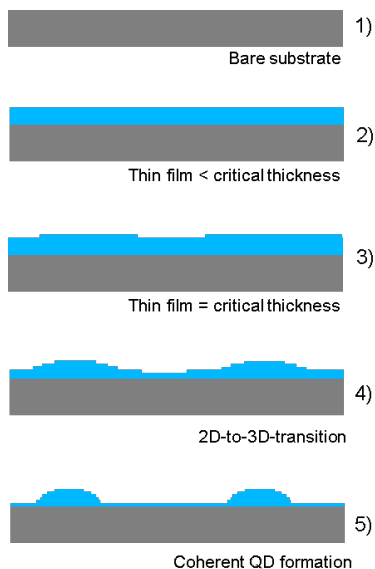
Figure 6. A schematic description of the QD formation mechanism.

2.2 Absorption spectroscopy

Absorption measurements were performed on samples with 45° polished facets in a multiple internal reflection geometry, schematically shown in Fig. 7. This allows for enhanced absorption but also enables coupling of light with the electric field in the growth direction into the structure. A Fourier-transform infrared (FT-IR) interferometer was used to measure the absorption.
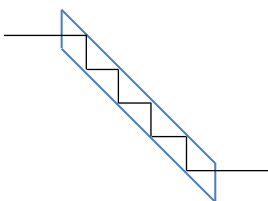
Figure 7. 45° polished facet multiple internal reflection geometry.

2.3 Photoluminescence- and photocurrent spectroscopy

The majority of the PL- and photocurrent measurements were done using a Bruker V70 FT-IR interferometer fitted with step-scan functionality and an MCT detector with 16 μm cut-off. The step-scan mode allows for lock-in amplification, effectively removing noise sources such as background thermal radiation. Normal-incident light was used to measure the photocurrent which

was pre-amplified in a Keithley 427 current amplifier before it was fed into the FT-IR electronics.

2.4 Scanning tunneling microscopy (STM)

Compared to TEM, STM is a surface sensitive technique where a tunneling current is measured between the sample surface and an ideally atomically sharp metal tip. The tunneling current is exponentially dependent on the tip-sample distance but also depends on the electronical properties of the surface [69]. The STM technique puts strict demands on the sample preparation with the requirement of atomically flat surfaces, preferably containing less than one atomic step per 50 nm surface, to allow for high quality images. The cross-sectional STM images presented in this work were measured from samples prepared according to the method of Ernerheim-Jokumsen and Reuterskiöld-Hedlund [70]. With this method, the samples get a 2-3 mm cut using a 0.2 mm-wide circular diamond saw and are thinned to 150 μm after which they are cleaved in-situ by forcing a knife into the cut. An Omicron VT-STM in a chamber with a base pressure lower than $1x10^{-10}$ mbar was used to record cross-sectional STM images at room temperature using W- and PtIr tips.

In addition, scanning-tunneling spectroscopy (STS) was performed with the feedback loop of the STM closed measuring I-V in each point. From the I-V spectra, the differential conductance dI/dV can be extracted which is proportional to the local density of states close to the surface [71]. Examples of differential conductance mapping performed on QD samples, where the QD eigenstates are imaged, can be found in Ref. [72, 73].

3 Theoretical background

3.1 Bandgaps of strained III/V materials

The most common model used to calculate the electronic properties of QDs is the **k·p** method [74]. It describes the electron distribution by envelope wave functions with the interaction between the bands treated via the **k·p** perturbation. A valid model relies on an accurate description of compositional and strain variations within the QD. While the latter can be calculated by means of the valence force field Keating model [75], continuum elasticity theory [76] or the Green's function technique [77], the two influence each other and are furthermore difficult to exactly determine by experiment. A closely related difficulty lies in determining some of the material parameters, such as the valence band offset between materials [78] on which even the most advanced of **k·p** models rely.

In this thesis we have used a simple model to calculate the strain- and composition dependent bandgap in III/V materials which serve as a guide in the bandgap engineering of the investigated QD materials. The model is based on the formalism of the **k·p** method and deformation potential theory in which we assume a QW-like strain, i.e. biaxial strain in the (001) crystal plane. In the case of the conduction band energy at the Γ-point for a cubic semiconductor, the strain-induced shift can be treated as a perturbation and be expressed as [79]

$$(3.1) \qquad \Delta E_C = 2a_c \left(1 - \frac{C_{12}}{C_{11}}\right) \epsilon_1$$

where a_c is the Pikus-Bir hydrostatic deformation potential, C_{11} and C_{12} are the elastic stiffness constants and ϵ_1 is the biaxial strain. The strain-induced shifts at the Γ-point in the coupled valence bands can similarly be obtained for the case of (001) biaxial strain in a cubic semiconductor. The following expressions are obtained from evaluating the 6-band **k·p** eigenvalue equation analytically [74]:

$$(3.2) \qquad \Delta E_{HH} = -(P_\epsilon + Q_\epsilon)$$

$$(3.3) \qquad \Delta E_{LH} = -P_\epsilon + \frac{1}{2}\left(Q_\epsilon - \Delta_{SO} + \sqrt{\Delta_{SO}^2 + 2\Delta_{SO}Q_\epsilon + 9Q_\epsilon^2}\right)$$

(3.4) $\Delta E_{SO} = -P_{\epsilon} + \frac{1}{2}\left(Q_{\epsilon} - \Delta_{SO} - \sqrt{\Delta_{SO}^2 + 2\Delta_{SO}Q_{\epsilon} + 9Q_{\epsilon}^2}\right)$

where $\epsilon_{11}= \epsilon_{22}=(a_{sub}\text{-}a_{epi})/a_{epi}$ is the biaxial strain defined by the substrate lattice constant a_{sub} and the epilayer lattice constant a_{epi}. Δ_{SO} is determined experimentally for unstrained material whereas P_{ϵ} and Q_{ϵ} can be expressed by

(3.5) $P_{\epsilon} = -a_v \left(1 + \dfrac{C_{12}}{C_{11}}\right)\epsilon_{11}$

(3.6) $Q_{\epsilon} = -b \left(1 + 2\dfrac{C_{12}}{C_{11}}\right)\epsilon_{11}$

a_v and b are the Pikus-Bir deformation potentials describing the influence of hydrostatic and uniaxial strain respectively. Notably, non-inverted hole energies are expressed in contrast to the formalism outlined by Ikonic [74].

The composition- and strain dependent Γ-point band edges were calculated from the aforementioned equations using tabulated values from [78] and linear interpolations of the ternary valence band offsets.

3.2 Photodetector figure of merits

In the following, we review some figure of merits used to define photodetector performance. Among these, D* is commonly used to characterize single-pixel detector elements whereas detector arrays are commonly compared in terms of noise-equivalent temperature difference (NETD).

3.2.1 Responsivity

The responsivity gives a measure of the photocurrent in relation to the optical intensity in the unit [A/W]. Assuming unity gain the responsivity is expressed as

(3.7) $R_I = \dfrac{q\lambda}{hc}\eta$ (A/W)

where q is the elementary charge, λ is the wavelength, h is Planck's constant, c is the speed of light and η is the quantum efficiency.

3.2.2 Noise

The noise plays an important role in defining the performance of a photon detector. The common noise sources are summarized by Kruse [80].

- Thermal noise (also called Johnson noise),
  originates from the random motion of carriers in a resistive material. The short circuit noise current is given by

$$i_T = \sqrt{\frac{4kT\Delta f}{R}}$$

  where k is Boltzmann's constant, T is the temperature, Δf is the noise bandwidth and R is the resistance of the sample being measured.

- Generation-recombination noise,
  is caused by fluctuations in the generation and recombination of charge carriers.

- Shot noise,
  originates in the discrete nature of the elementary charge and the random arrival at the contacts. In a reverse biased photodiode it expresses itself as

$$i_S = \sqrt{2qI_0\Delta f}$$

  where q is the elementary charge, I_0 is the saturation current and Δf. Shot noise is also present in a photon flux.

- 1/f-noise (also called flicker noise),
  gives a significant contribution at low frequencies. Its origin is generally not known but it appears to be associated with the presence of potential barriers at contacts, in the interior or at semiconductor surfaces.

3.2.3 D*

D* (pronounced dee-star) is an important parameter used to assess the signal-to-noise performance in photodetectors. For a monochromatic radiation source it is expressed as [81]

(3.8)
$$D^*(\lambda) = \frac{R_I}{\frac{i_{noise}}{\sqrt{A\Delta f}}} = \frac{\frac{q\lambda}{hc}\eta}{\sqrt{\frac{i_d^2}{A\Delta f} + \frac{i_b^2}{A\Delta f}}} \qquad \left(\text{cmHz}^{1/2}/\text{W}\right)$$

where R_l is the responsivity, i_{noise} is the total current noise, A is the detector area, i_d is the dark current noise and i_b is the shot noise of the background photon flux in the detector scene.

A special condition occurs when the background noise equals the dark current noise. At this condition, the so-called background limited photodetector (BLIP) condition D* in a photovoltaic detector can be expressed as [82]

$$(3.9) \qquad D_{BLIP}^*(\lambda) = \frac{\lambda}{hc}\sqrt{\frac{\eta}{2\Phi_B}} \qquad \left(\text{cmHz}^{1/2}/\text{W}\right)$$

D* can also be expressed in response to a black body source as a function of the black body temperature T. Unless otherwise stated, the detector field of view is assumed to be hemispherical (2π steridians). D* in this case is expressed as [80]

$$(3.10) \qquad D^*(T) = \frac{\sqrt{A\Delta f}}{P}\left(\frac{i_{photo}}{i_{noise}}\right) \qquad \left(\text{cmHz}^{1/2}/\text{W}\right)$$

where A is the detector area, P is the incident radiant power, i_{photo} is the photocurrent and i_{noise} is the root-mean-square current noise.

3.2.4 Noise-equivalent temperature difference (NETD)
A measure often used to assess the performance of focal plane arrays is the noise-equivalent temperature difference (NETD). It is defined by [83]

$$(3.11) \qquad NETD = I_n \frac{\Delta T}{\Delta I_s} \qquad (\text{mK})$$

where I_n is the root-mean-square noise and ΔI_s is the signal measured for the temperature difference ΔT. The NETD can be modeled if the I-V characteristics and the spectrally dependent quantum efficiency are known. First, the spectral radiance of a blackbody corresponding to the detector scene temperature is calculated from Planck's law as

$$(3.12) \qquad B = \frac{2hc^2}{\lambda^5}\frac{1}{e^{\frac{hc^2}{\lambda kT}}-1} \qquad \left(\frac{\text{W}}{\text{Sr}\cdot\text{m}^2\cdot\text{m}}\right)$$

which can be expressed in terms of photons per second by multiplication with $\lambda/(h \cdot c)$

$$(3.13) \qquad B_{ph} = \frac{2hc^2}{\lambda^5} \frac{1}{e^{\frac{hc^2}{\lambda kT}} - 1} \cdot \frac{\lambda}{hc} \qquad \left(\frac{\text{photons}}{\text{s} \cdot \text{Sr} \cdot \text{m}^2 \cdot \text{m}}\right)$$

The portion of the spectral radiance which is perceived by the detector focal plane array behind a cold shield aperture or a lens with a focal length to diameter ratio $f/\#$ is called the spectral irradiance E and can be expressed in a simple model as [83]

$$(3.14) \qquad E_{ph} = \frac{1}{1 + 4\,(f/\#)^2} \cdot B_{ph} \qquad \left(\frac{\text{photons}}{\text{s} \cdot \text{m}^2 \cdot \text{m}}\right)$$

The spectral irradiance is calculated in Fig. 8 for an f/4 aperture and a background temperature of 30 °C. Here we see the spectral irradiance expressed in terms of photon flux as a function of wavelength. Notably for this background temperature, which corresponds to the temperature of a typical imaged object, the majority of the photons have wavelengths longer than 5 μm.
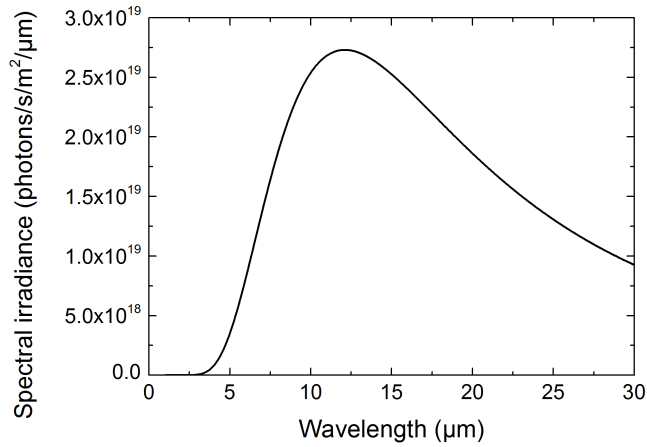
Figure 8. Calculated spectral irradiance for f/4 optics and a background of 30 °C.

Multiplying the spectral irradiance with the wavelength-dependent quantum efficiency gives the spectral photocurrent density which is plotted for a type-II $In_{0.5}Ga_{0.5}Sb$ QD photodetector material in Fig. 9. Here the spectral photocurrent density is plotted as a function of wavelength.

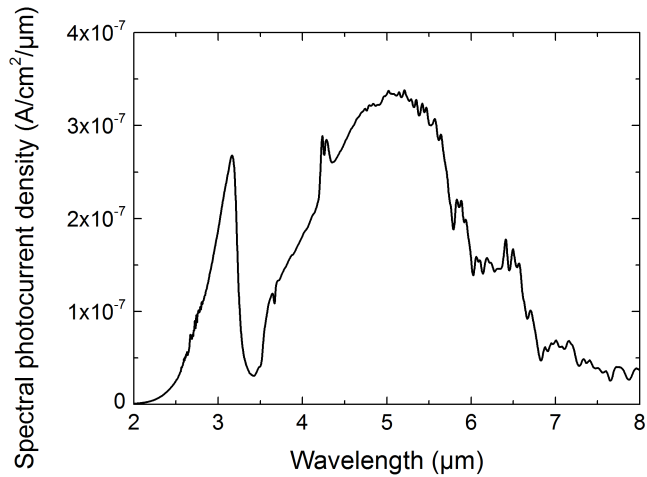**Figure 9. Spectral photocurrent of a type-II $In_{0.5}Ga_{0.5}Sb$ QD photodetector based on measured quantum efficiencies at 196 K. The calculation assumes an f/4 aperture and a 30 °C background.**

The detector photocurrent density can be calculated by integrating the spectral photocurrent over the desired spectral range.

An important parameter for the NETD calculation [84] is the thermal contrast C which expresses the fractional change in detector output per change in scene temperature.

$$(3.15) \qquad C = \frac{1}{I_{\det}(T_{scene})}\left(\frac{\partial I_{det}(T_{scene})}{\partial T_{scene}}\right) \qquad (1/K)$$

The NETD can be calculated from the scence temperature difference which corresponds to a change in the photocurrent equal to the noise [85] :

$$(3.16) \qquad NETD = \left(\tau C \eta_{BLIP}\sqrt{N_w}\right)^{-1}$$

Here τ is the optics transmission factor which often can be assumed to be close to unity and N_w is the number of carriers photogenerated within the integration time t_{int}:

$$(3.17) \qquad N_w = \eta A_d t_{int} E_{ph}$$

The "percentage of BLIP", η_{BLIP}, is the ratio of photon noise to composite pixel noise [85]

$$(3.18) \qquad \eta_{BLIP} = \sqrt{\frac{N_{photon}^2}{N_{photon}^2 + N_{pixel}^2}}$$

In Eq. (3.16) we note that the NETD is inversely proportional to the square root of the photogenerated carriers which correspond to the integrated charge in the ROIC capacitor. Hence, the NETD benefits from high quantum efficiency and a long integration time.

4 (Al)GaAs(Sb)/InAs QDs

Although epitaxial self-assembly of QDs is most commonly associated with growth of compressively-strained materials, tensile-strained QDs, also referred to as "anti-dots", have been demonstrated for a number of III/V-material combinations [64, 86, 87, 88, 89, 90, 91, 92]. References [90] and [92] furthermore show photoluminescence and lasing of GaAs QD/GaSb heterostructures respectively. This suggests that tensile strained QDs can be grown coherently and can be optically active. Of particular interest for this thesis are GaAs-based QDs grown on InAs (0 0 1), which are predicted to have an effective type-II bandgap matching the MWIR and LWIR spectral regions [93], [Paper A]. An attractive property of tensile strained QDs is that the highest valence band states are light-hole like. Since this implies a lower effective mass of the holes, it is expected that the corresponding wave functions penetrate deeper into the matrix as compared to heavy hole states [94]. This entails an increase in the wave function overlap between conduction band and valence band states resulting in a higher absorption coefficient, which is beneficial for photon detection. In this thesis we have explored the possibility of realizing photodetectors for the LWIR spectral region based on (Al)GaAs(Sb) QD grown in an InAs matrix.

4.1 The influence of Si doping on absorption

As discussed in Paper A, we identify absorption properties in (Al)GaAs(Sb)QD/InAs structures which follow the expected behavior of intra-valence band absorption with distinct peaks in the MWIR and the LWIR infrared ranges; The absorption energy decreases for reduced QD layer thickness as well as for increased QD bandgap by the alloying with AlAs. Strikingly, these properties are only observed for Si-doped QDs. Intra- valence band absorption is expected when there is a presence of bound holes in the QDs, as in the case of e.g. p-doped QDs. Under normal circumstances however, Si provides n-type doping in GaAs. A possible explanation for the observed phenomenon can be that the QDs indeed are p-doped as it has been shown that Si can take the As lattice site and provide p-doping in GaAs for growth on crystal planes other than the standard (001) [95, 96, 97]. Several facets are present during island growth, which may influence the Si-incorporation and result in p-type material. The high tensile strain can also possibly have an influence on both the incorporation and the dopant energy level. Alternative dopant materials from group II (Zn) and group VI (Te) , in the form of DEZn and DETe were investigated using nominal dopant concentrations from 5×10^{18}

31

cm^{-3} to 1×10^{22} cm^{-3} and 5×10^{17} cm^{-3} to 1×10^{19} cm^{-3} respectively. However, no QD-related absorption was observed in either case. So far no conclusion can be drawn on the role of Si-doping and the absorption of (Al)GaAs(Sb) QD/InAs structures remains poorly understood.

4.2 Photoluminescence spectroscopy of (Al)GaAs(Sb) QDs

Single- and multilayer structures with (Al)Ga(Sb) QD layers of nominal thickness in the range 1.2-5 MLs were measured by means of PL spectroscopy at 77 K and 4 K. In all cases, no quantum dot related PL could be observed although luminescence stemming from the InAs matrix is detected. This suggests either that the heterostructure lacks a confining potential, which is inconsistent with the observed absorption and contradictive to the band edge calculations, or alternatively, the radiative recombination path is too inefficient. The former was claimed by Tenne *et al.* without a full motivation [88]. On the other hand the band edge calculations made in Paper A and by Pryor and Pistol [93] are both based on the composite value of the GaAs/InAs valence band offset presented by Vurgaftman *et al.* [78]. The valence band offset was chosen from values in a range of 0.29 eV. Notably, this is comparable to the bandgap of InAs and constitutes a probable error. The calculations furthermore assume strain distributions which may differ from the grown material, where dot geometry and interdiffusion with the matrix material can play a major role. However, absence of radiative recombination can also be a result of more efficient competing non-radiative recombination paths [98]. Such non-radiative recombination paths are often facilitated by crystal defects [98]. The growth conditions used in this thesis can have induced crystalline defects. Moreover could these be inherent to the material combination.

A relevant study in this context was presented by Ohkouchi and Ikoma [87]. In their work they epitaxially deposited GaAs on nominal and vicinal InAs (001) surfaces. They observed that InGaAs clusters form near step edges which relax strain by formation of cracks whereas GaAs deposited on a flat surface relaxes strain by forming 3D islands. According to this conclusion low-temperature epitaxy could reduce adhesion to step edges and thereby possibly improve crystal quality. In addition, growth on exactly oriented wafers or alternatively, buffer layer growth at high temperature can possibly provide better conditions for formation of defect free, coherently strained QDs.

In summary, absorption in tensile strained (Al)GaAs(Sb) QD/InAs structures was observed with intraband-like behavior. The measured absorption energies

indicate that the material can be suitable for infrared detection. Tensile strained QDs are potentially better suited for detection than their compressively strained counterpart due to their light hole –like confined states.

5 In(Ga)Sb/InAs QDs

InSb QDs with spontaneous emission in the MWIR spectrum were first demonstrated by Norman et al. [99]. These were, in contrast to the original work on self-assembled InSb QDs by Glaser et al., grown on InAs substrates, which at the time provided the smallest interband transition energy in any epitaxially self-assembled QD system [100]. This is due to the band alignment with InAs which forms a type-III heterojunction; i.e., there is no overlap of the bandgaps of the two materials [78]. Such a configuration is highly attractive for infrared photon detection since its interband transitions could in theory span the whole IR range. An essential part of this thesis is focused on developing MOVPE growth methods to decrease the optical transition energies in this heterojunction and to realize a sensor material with response in the LWIR spectrum [Paper B, Paper C, Paper D].

5.1 Band energies

Figure 10 shows the calculated conduction and valence bands of InGaSb alloys biaxially strained to InAs (001). The type-III band alignment is preserved for the whole range of compositions while the strain varies from 7% for InSb to 0.6% for GaSb. The photoluminescence reported in InSb QD/InAs material stems from recombination between continuum electron states in InAs and bound hole states in the QDs [99, 65, 101, 102, 103, 104][Paper B]. The emission wavelength is strongly dependent on the confinement effects in the QDs predominantly defined by the QD size, as argued in Paper B and Paper C. In the course of this thesis several growth parameters were studied, such as nominal thickness, V/III ratio, temperature, growth rate and growth interrupts, in order to obtain larger quantum dots suitable for the LWIR waveband.
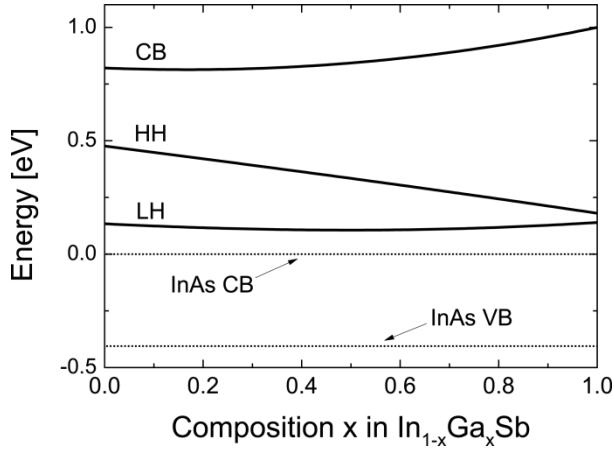
Figure 10. Calculated conduction band minima and valence band maxima at the gamma point for biaxially strained InGaSb alloys grown on InAs (001) at 77 K.

5.2 Growth optimization

In the framework of developing In(Ga)Sb QD growth, AFM characterization of uncapped QD layers revealed nanometer height variations on micrometer length scales. A discrepancy between AFM measurements of uncapped QDs and PL measurements on capped QDs was previously identified for samples grown in the Aixtron 200/4 reactor at KTH in the InAs QD/GaAs and GaSb QD/InAs material systems. This can be explained by material redistribution in the test samples during reactor cool-down or it could indicate that the capping plays a role in the QD formation which is known in e.g. the InAs QD/GaAs material system [105, 106, 107, 108] . For this reason bulk of the optimization was done based on PL measurements. The QD-like shape of the grown structures was confirmed by STM measurements.

5.2.1 InSb QDs

The optimization of InSb QD growth conditions for long wavelength is described in Paper B. Here it was found that nominal QD layer thickness, the V/III ratio in the inlet gas phase and temperature were the most influential growth parameters. Particularly temperature is known to strongly influence QD formation; both the nucleation phase and the 3D-island growth phase are thermally activated [59, 109]. The rationale of the study was, hence, to find an optimal growth temperature which promotes growth of large QDs in this material. To investigate and find optimum conditions for large-QD formation a

number of single-QD-layer samples capped with 50 nm InAs were grown in the temperature range 430-530 °C. Figure 11 summarizes the PL measurements of these samples showing PL intensity as a function of energy and wavelength [partially shown in Paper B, Fig. 3] Independently of the growth temperature we observe a luminescence peak at approximately 3 μm stemming from the InAs matrix. In addition, PL originating from type-II transitions in the QDs is observed in the range 4.3-6.2 μm. Interestingly, the transition energy shows a pronounced redshift while increasing the growth temperature from 430°C to 450°C with a subsequent blueshift up to 530°C. Furthermore, at growth temperatures between 450°C and 490°C the luminescence shows a double peak structure indicating a second bound state or a bimodal distribution of island sizes. The longest wavelengths are obtained for the temperature range 450-490 °C. There are several reasons which can explain this temperature behavior. While it is expected that growth at high temperature would facilitate diffusion of adatoms promoting growth of large QDs, the nucleation process is simultaneously facilitated. The short PL wavelengths in the high temperature samples can indicate that the island evolution is strongly influenced by the initial nucleation. Alternatively, it can also be explained by interdiffusion with As which increases the type-II bandgap. The short PL wavelengths for the samples in the low-temperature regime can be explained by a limited adatom surface mobility or influence of the precursor chemistry at low temperature, although it has been reported that TMSb can be catalytically decomposed on surfaces in the presence of TMIn at 400 °C [110]. In summary, we found that InSb QDs deposited at 450 °C-490 °C have the lowest transition energy for the specific growth conditions which makes them a suitable base for further optimization. 470 °C was chosen as growth temperature due to a higher PL intensity of the QDs relative to the matrix.
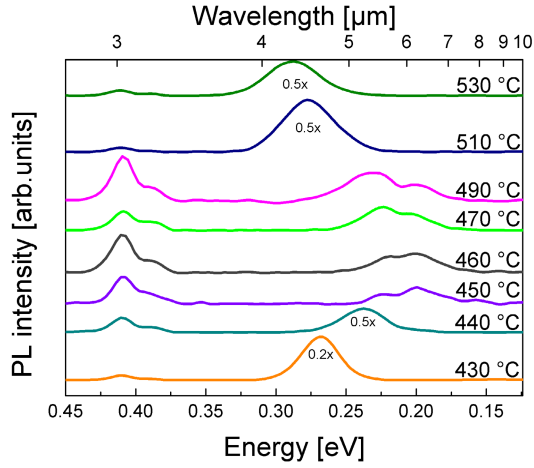
Figure 11. Photoluminescence at 77 K of single-layer InSb QD samples grown in the temperature range 430-530 °C at a nominal thickness of 5 ML and 0.8 as the V/III ratio. The curves have been offset for increased readability. Four of the curves have been scaled down for the same reason. 36 mW excitation power was used in the measurement.

In addition to the growth optimization reported in Paper B, the influence of growth interrupts (GIs) on the QD formation was investigated. Growth interrupts can increase the dot height and, hence, red-shift the PL in the more common QD systems InAs/GaAs and InAs/InP [111, 112, 113]. For this study, a series of samples was fabricated with GIs during and after the QD layer deposition. Three samples were prepared with a 10 s GI after the following portion of the QD layer was deposited: one quarter, one half and the full QD layer. After the GI the full QD layer deposition was completed (8 ML) and the sample was capped. Another two samples were prepared with GIs after the QD layer deposition; one with a 30 s GI and one with a 10 s GI during which the surface was stabilized with Sb. Figure 12 displays a waterfall plot of the PL intensity as a function of transition energy and wavelength of these samples where the topmost sample grown without GI is added as a reference. The samples subjected to GIs before the full QD layer deposition show a very small shift in the QD-layer-related PL peak wavelength. This can be an indication that the critical thickness is less than 4 ML. Furthermore, a significant blueshift of the type-II transition is observed for the 10 and 30 s GI samples where the Sb-stabilized sample notably displays a smaller shift. This is interpreted as a redistribution of material into smaller islands and can be explained by an equilibrium density and QD size which differs from the density defined by the initial nucleation. If so, a slowing of the kinetics can be advantageous for large

37

QD formation. Antinomy stabilization of the surface is possibly an example of this.
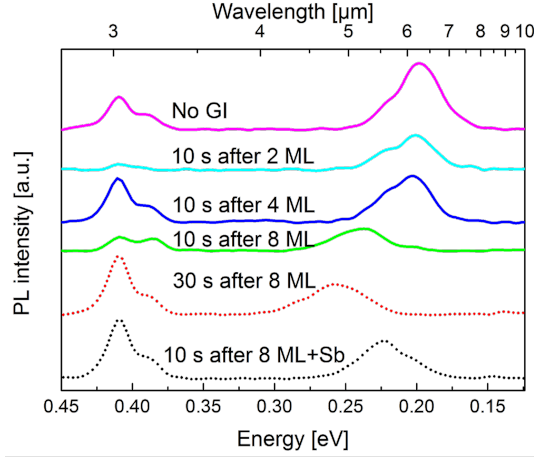

Figure 12. Photoluminescence at 77K from single-layer InSb QD samples grown with different GI sequences. The QD layers are nominally 8 ML grown at 470 °C and 0.8 as V/III ratio. The excitation power was 36 mW.

The optimal parameters found for growth of long-wavelength single-layer InSb QDs with peak PL at 6.2 μm are: 8 ML nominal thickness, V/III=0.8 and a growth temperature of 470 °C without any GI. Multilayer growth of this material was investigated with InAs spacer thicknesses of 50 nm in order to isolate the stress in the QD layers. It was found that samples with 5 QD layers had a rough surface morphology and decreased peak PL intensity which was related to poor quality of the matrix material growth at the QD growth temperature 470 °C. High quality growth of InAs was achieved at 530 °C and this was also employed in growth of multilayer QD samples by an initial 5 nm cap of the QDs at the QD growth temperature after which 45 nm InAs was deposited at 530 °C. The difference of the two capping methods is displayed in Fig. 13 where we plot the PL intensity as a function of the transition energy and the corresponding wavelength. We find that the high-temperature capping increases the QD peak PL intensity by roughly three times.
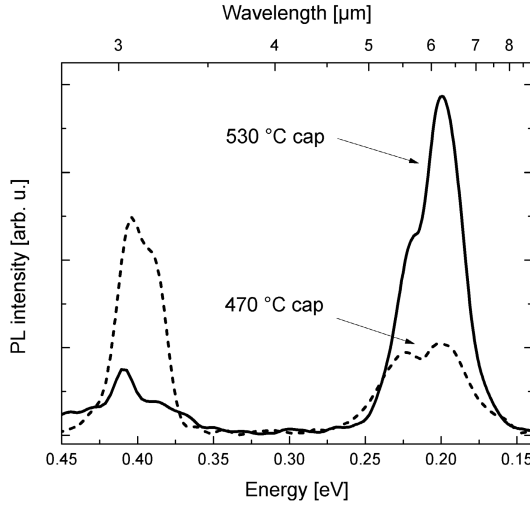
Figure 13. Photoluminescence at 77 K from 5-QD-layer InSb samples with InAs spacer layers grown at 470 °C and 530 °C. The excitation power was 36 mW.

With the described method, high quality multilayer InSb QD samples were grown with up to 20 layers. The PL from these samples, displayed in Fig. 14 as a function of energy and wavelength, shows a negligible shift of the peak PL wavelength and very little broadening with increasing number of layers. This indicates that the spacer layer is sufficiently thick and of sufficient quality not to influence the growth of subsequent QD layers. This growth scheme was used in the fabrication of the photodetectors demonstrated in Paper B.
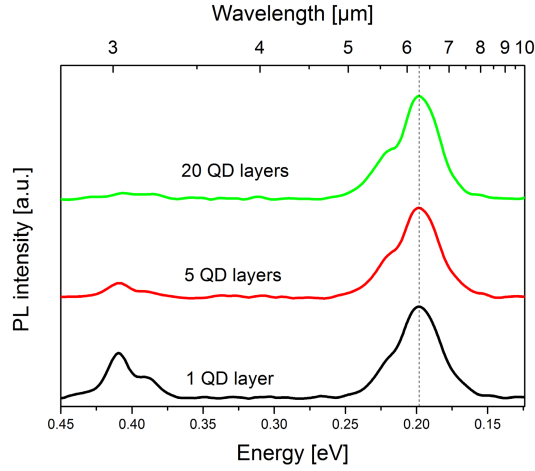
Figure 14. Photoluminescence at 77 K of samples containing multiple layers of InSb QDs grown at 470 °C with InAs spacer layers grown at 530 °C. The QD layer nominal thickness is 8 ML and the V/III ratio during QD growth was 0.8. The excitation power was 36 mW.

5.2.2 InGaSb QDs

Paper C describes how the growth of InGaSb QDs is optimized for long wavelength. Here we argue that the addition of Ga in the QDs has a moderate effect on the band energies, as can be seen in Fig.10, and a large effect on the QD growth dynamics due to lower strain which is interpreted to result in formation of larger QDs with less confinement effects. It is observed that a higher temperature and a larger nominal QD layer thickness are needed for formation of long-wavelength InGaSb QDs as compared to pure InSb QDs. An example of this can be seen in Fig. 15 (Paper C, Fig. 6) which displays the photoluminescence of a series of single-QD layer samples grown at 530 °C. Here PL is demonstrated up to 12 μm for 16 ML $In_{0.4}Ga_{0.6}Sb$ QDs. A general remark is that the PL intensity decreases with increasing emission wavelength. This can either be explained by nucleation of dislocations that increase the non-radiative recombination or by a reduction of wave-function overlap as a result of the weaker confinement.
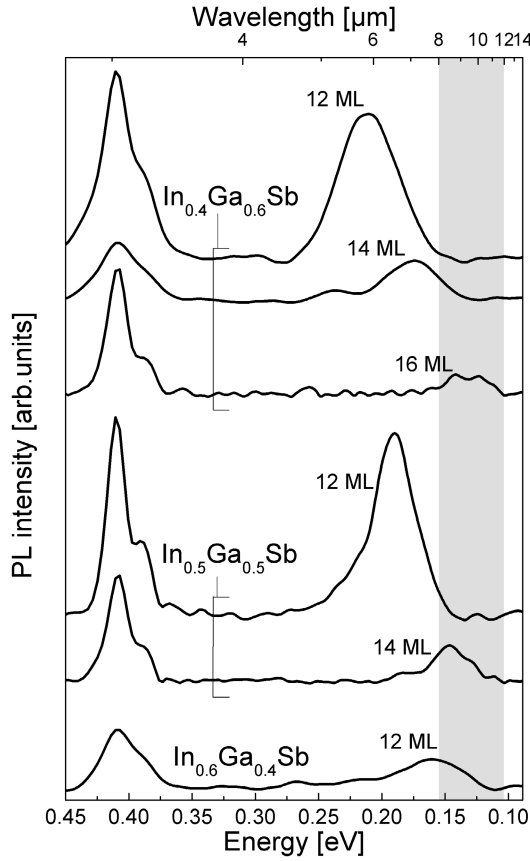
Figure 15. Photoluminescence at 77 K of single-layer InGaSb QD samples grown with varied thickness, composition at 530 °C with a V/III ratio of 1.2. 67 mW excitation power was used in the measurement.

As the total volume of the material in a QD layer is small compared to the absorber volume in a bulk material based photodetector, in which the absorber region can be several micrometers thick, it is expected that multiple QD layers are required to allow for good absorption. Therefore, growth of InGaSb QD multilayer structures was studied in test structures where 10 QD-layers are grown with 80 nm spacer layer thickness on a 200 nm InAs buffer layer. Of particular importance is how the material accommodates the strain and how the topmost QD layers are affected by the initially grown QD layers. This is illustrated by the photoluminescence spectrum in Fig. 16, which shows the PL intensity as a function of energy and wavelength for multilayer QD samples grown under different conditions. In this figure, the peak PL of the 10-

41

layer samples is shifted to longer wavelength as compared to the single-layer samples. The shift is larger for the case of 12 ML $In_{0.5}Ga_{0.5}Sb$ QDs compared to 14 ML $In_{0.4}Ga_{0.6}Sb$ QDs. Clearly, the growth of multiple QD layers is affecting the optical properties of the material which is possibly a result of initial QD layers acting as stressors for upper lying QD layers, roughening of the surface as a consequence of the 3D growth, or non-elastic strain relaxation. Notably, Nomarski phase-contrast micrographs of the surfaces from the samples in Fig. 16a and b are specular and are not significantly different from the surfaces of epitaxially grown InAs layers with comparable thickness. The QD growth parameters from Fig. 16 (a) were used in the fabrication of the photodetectors presented in Paper D.
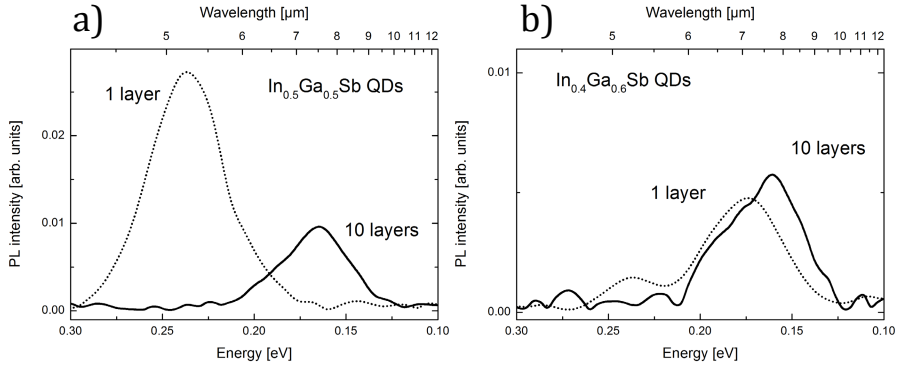

Figure 16. Photoluminescence at 77 K of multilayer InGaSb QD samples grown at 530 °C, V/III ratio 1.2 with a) 12 ML $In_{0.5}Ga_{0.5}Sb$, b) 14 ML $In_{0.4}Ga_{0.6}Sb$. An excitation power of 67 mW was used.

To further evaluate the influence of the nominal QD-layer thickness of multilayer samples we reproduced the 10-QD-layer sample of Fig. 16 (a) with an increased QD-layer thickness to 14 ML. The resulting PL spectroscopy data is plotted in Fig. 17 (a). Here we see PL as a function of energy and wavelength with QD peak PL intensity at 9 µm. Due to a very weak PL signal twice the excitation power of the measurement in Fig. 16 (a) was used. Still, the PL intensity is about half of that in Fig. 16 (a). Additionally Fig. 17 (b) shows the Nomarski phase-contrast micrograph of the corresponding sample. The surface morphology shows a large number of micrometer-sized defects and has a "milky" or "hazy" appearance which is interpreted to be a result of non-elastic strain relaxation. It illustrates that growth of multilayer InGaSb QD structures aimed for the LWIR is very sensitive to small variations of the growth parameters which in turn indicates a close proximity to the critical point of plastic strain relaxation. Thus, the growth of 50 or 100 QD-layers,

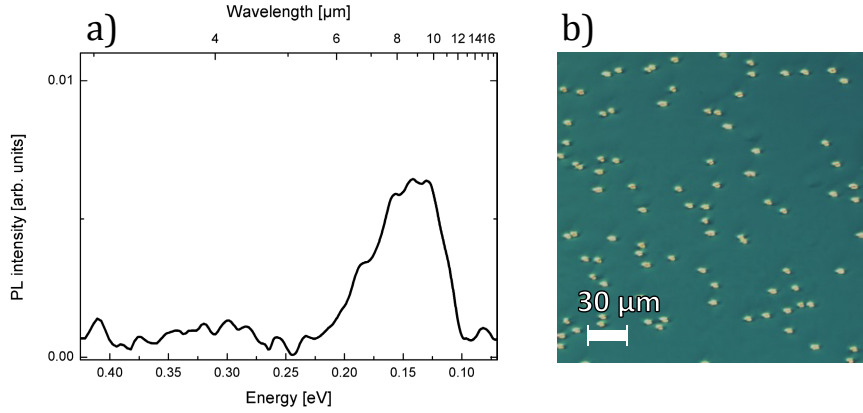potentially attractive for high quantum-efficiency photodetectors, can prove to be a significant challenge

Figure 17. Properties of a 10 layer sample consisting of 14 ML QD layers of In$_{0.5}$Ga$_{0.5}$Sb studied with a) Photoluminescence (77K) at 146 mW excitation power and b) Nomarski phase-contrast microscopy. The sample was grown at 530 °C with a V/III ratio of 1.2 with 80 nm InAs spacer layers.

5.3 Microscopy

A key point in the development of long-wavelength type-II QD material is the relation between the theoretically predicted band alignment and the actual measured type-II transition. The simple strained thin-film model used in this thesis predicts that the dots must provide strong confinement to match the measured photoluminescence energies [Paper B, Paper C]. Microscopy can be a powerful tool to investigate structural properties of QDs such as size and shape but also crystal defects and to some extent compositional variations stemming from e.g. intermixing or segregation [114, 58, 115]. Norman *et al.* and Ivanov *et al.* reported transmission electron microscopy (TEM) results on InSb QD/InAs heterostructures grown with MOVPE and molecular-beam epitaxy (MBE), respectively. The measured dot diameters were in the range 2.5-10 nm which suggests that the QDs have strong confinement effects [99, 101] .

5.3.1 Transmission electron microscopy (TEM)
In the course of this work, several attempts were made to image InSb QDs with TEM. For plan-view samples, dimpling and argon ion milling was used to prepare samples while cross-section samples were prepared with focused-ion-beam (FIB) and gallium ions as sputter medium. In both cases it was found that the sample preparation introduced disturbing elements for the measurement. For the FIB-prepared samples this is likely related to the sputtering damage

caused by gallium ions and in the argon milled samples redeposition of sputtered material is identified as a probable source. The disturbances are particularly worrisome for plan-view measurements and the alignment procedure for weak-beam dark-field condition which is commonly used to image strain and dislocations with high contrast [116].

The cross-section TEM micrographs obtained, an example of which is displayed in Fig. 18, show results comparable to what was reported by Ivanov *et al.* [101]. The figure shows the cross section of three dot layers indicated by dark contrast. These layers are separated by 80nm of InAs. As with the cross-section TEM results from Ivanov *et al.*, the individual QDs in this figure are difficult to discern; partly due to the spotty pattern identified as sputtering damage but possibly also due to small dot sizes.
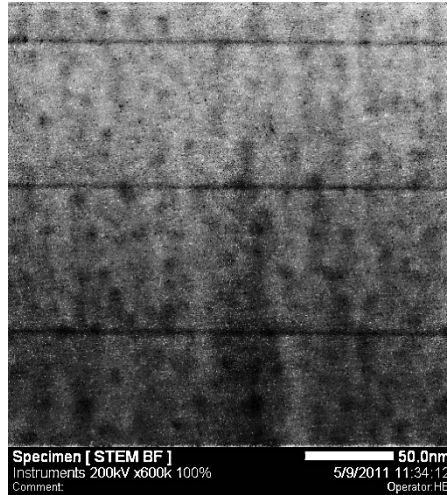

Figure 18. Cross section bright-field STEM micrograph of an InSb QD multilayer structure consisting of 10 QD layers, each 3 ML thick. The sample was grown at 490 °C at with V/III ratio 1.6.

5.3.2 Scanning tunneling microscopy (STM)

A major milestone of this thesis work was the confirmation by STM that QDs had formed with the here presented growth method [Paper B, Fig. 6]. This figure describes a layer with morphological and compositional variations strongly confined in the growth direction which is interpreted to be a result of

QD formation with dimensions in line with the TEM microscopy results of Norman *et al.* and Ivanov *et al.* [99, 101].

Additional measurements were performed on samples with longer PL wavelengths which proved to be more difficult to image with atomic resolution. Atomic resolution of the matrix material was achieved multiple times but the QD layer was always blurred. A possible reason could be a disturbance of the tip due to large bulging of the QD layer caused strain release after cleaving. It could also originate in the increased offset between the bound hole states and the valence band edge which is probed when atomic resolution of the matrix is achieved. Due to the band alignment, all QD states are probed when probing the matrix valence band. Since these states can have different localization, it can influence the resolution in a negative way.

In this work we have performed STS measurements on cross-sections of an $In_{0.5}Ga_{0.5}Sb$ QD layer of which the differential conductance is imaged for a number of sample biases in Fig. 19. The sample bias is swept to larger negative values from top to bottom, imaging filled states. Filled states available for tunneling are schematically indicated in green on the left hand side in the figure. At V_{sample}=-0.07 V no contrast between the QD layer and the matrix can be seen which is interpreted as probing of states in the bandgap of both materials. When the bias is changed to -0.13 V, the conductance from the QDs can be differentiated which possibly corresponds to the QD ground state. The QD signal increases with increasing negative sample bias indicating that an increasing number of states are probed. At -0.35 V higher, less localized QD states and possibly also quasi-continuum states are probed. In this image the individual QDs can no longer be identified and the QD layer appears as an undulated QW. The interpretation of this measurement series is that QDs have formed also in the case of $In_{0.5}Ga_{0.5}Sb$ which appear larger than InSb QDs as measured in constant-current "topography" mode STM.

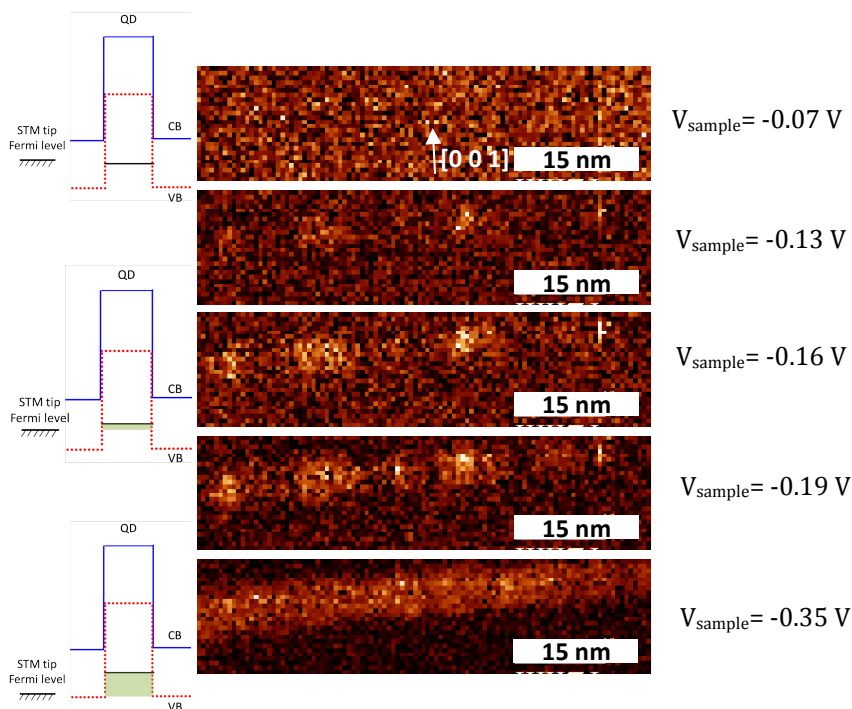**Figure 19. Normalized conductance images [(dI/dV)/(I/V)] of an In$_{0.5}$Ga$_{0.5}$Sb QD layer cross-section with 12 ML nominal thickness grown at 530 °C with V/III ratio 1.2. Schematics of the band structure are shown on the left hand side with filled states available for tunneling indicated in green and the ground QD state indicated in black. The tip scanning was done in the vertical image direction. The sample bias is varied in the range -0.07 to -0.35 V from top to bottom. The growth direction is upwards in the figures as indicated.**

An additional STS study was performed on a sample from the same wafer, this time including positive sample biasing to image empty states, presented in Fig. 20. The tip conditions were not as good as for the measurement in Fig. 19 and there was some drift in the piezoelectric actuators during the data capture as evidenced in the QD layer positioned diagonally across the images. The sample bias was swept from -0.85 V to +1.1 V. At the highest positive sample bias both the InAs matrix and the QD layer show signal, which means that there are free electron states available at the probed energy level. These empty states available for tunneling are schematically indicated in blue on the left hand side of the figure. When the sample bias is lowered to 0.18 V the matrix signal is still there but the QD signal disappears. Since no electrons can tunnel into the QD layer, we interpret this to correspond to energies above the QD ground state. When the bias is furthermore lowered to -0.09 V the signal from the

matrix disappears, which suggests that probing of states within the bandgap of InAs but above the QD ground state occurs. At -0.37 V sample bias, the bound QD states are probed with little signal from the matrix. At higher negative sample bias (-0.85 V) tunneling to the matrix valence band dominates. This study provides a qualitative measure of the band alignment in the $In_{0.5}Ga_{0.5}Sb$ QD/InAs heterostructure and strongly indicates that the heterostructure is either of type-II or type-III in accordance with the band edge calculations presented in Fig 10.
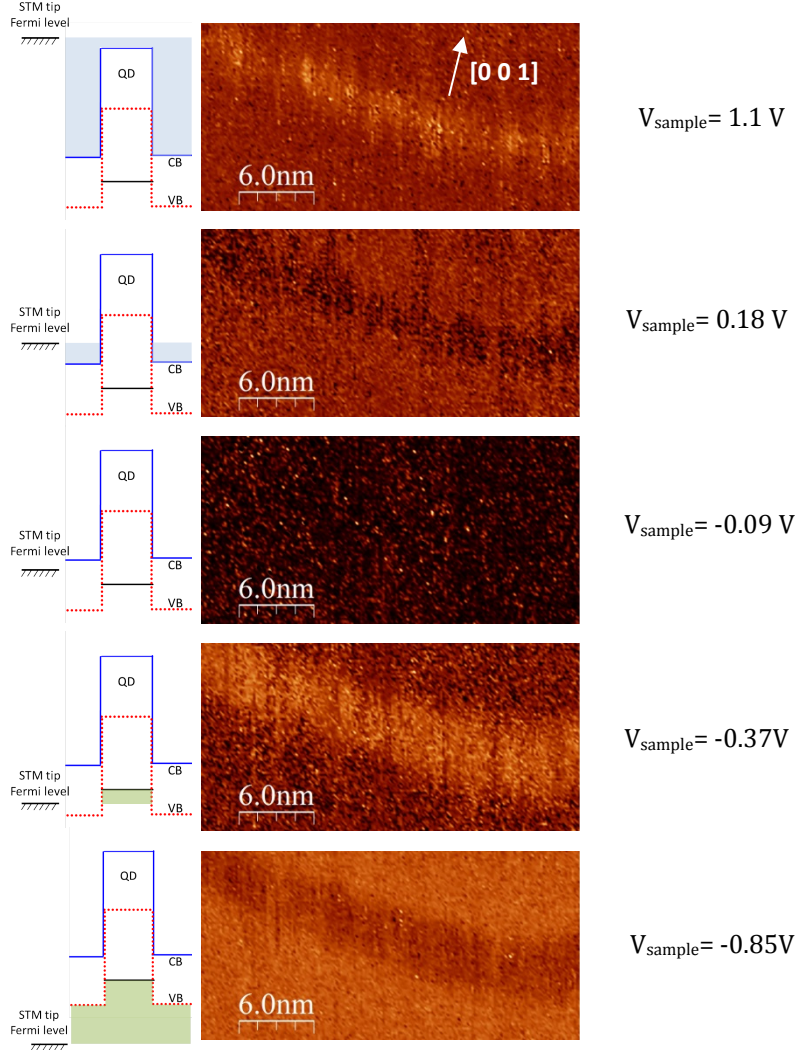
Figure 20. Normalized conductance [(dI/dV)/(I/V)] images of an In₀.₅Ga₀.₅Sb QD layer cross-section with 12 ML nominal thickness grown at 530 °C with V/III ratio 1.2. Schematics of the band structure are shown on the left hand side with empty states available for tunneling indicated in blue, filled states available for tunneling indicated in green and the ground QD state indicated in black. The tip scanning was done in the vertical image direction. The sample bias is varied in the range 1.1 V to -0.85 V from top to bottom. The growth direction is upwards in the figures as indicated.

6 In(Ga)Sb type-II QD photodetectors

Near-IR photodetection mediated by type-II transitions in epitaxially grown self-assembled QDs has been reported in several instances and has a potential application in intermediate-band gap solar cells (IBSCs) [117, 118, 119, 120, 121]. Detection at longer wavelengths, suitable for infrared imaging, has so far only been demonstrated by two groups [122, 123] [Paper B, Paper D]. In this work the aim has been to fabricate photodetectors for the LWIR spectrum compatible with standard indium-bump FPA hybridization techniques involving a mesa-etch to define pixels [124]. We have employed an iterative approach of extending the detection wavelength in subsequent QD photodetectors based on the progress of the QD material development outlined in section 5.2.

6.1 Design and fabrication

A simple p-i-n diode design was devised to evaluate multiple In(Ga)Sb QD layers in an InAs matrix as optical active material in photodetectors. A schematic model of the band diagram of the here presented QD photodiodes is shown in Fig. 21 indicating the energy levels in the QDs and the QD bandgap which has a type-III alignment with the InAs matrix. The light-blue arrows indicate the type-II optical excitation path, generating electrons in the conduction band and holes in the QDs. The diode design was chosen over a photoconductor design to relax the needs for accurate control of the intrinsic layer carrier concentration, which is known to be difficult to measure in InAs using standard techniques [125].
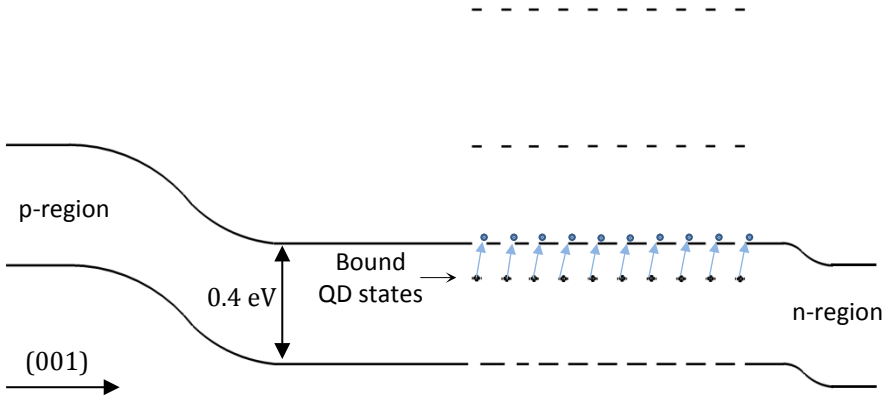
Figure 21. Schematic of the band edges in a 10 QD layer photodetector p-i-n diode indicating the photocurrent generation mechanism

Three batches of photodetectors are presented in this thesis, each with subsequent improvements in the device design and fabrication methods where particularly the growth conditions of the QD layers are different. The layer structures of the three detectors are presented in Fig. 22. In the first batch (a) the matrix material was grown at 490 °C. The distance of the junction and the closest QD layer is 250 nm. In the second batch (b) the growth temperature of the matrix was increased to 530 °C based on the findings in section 5.2.1. Moreover, the spacing between QD layer and the pn-junction was increased to 800 nm to minimize potential band-to-band tunneling through the QD states, analogous to trap-assisted-tunneling [126]. In the final batch (c) the layer structure was inverted to n-i-p which is compatible with the available read-out circuit (ROIC) ISC 9705. In addition, a thin highly-doped p-layer was added on top to facilitate the formation of an ohmic contact. As reported by Millea *et al.*, the p-InAs/metal interface can form a full-inversion barrier due to Fermi level pinning in the InAs conduction band, which acts with rectifying effect in the reverse bias direction [127].

Figure 22. Layer structures of the presented devices. The activate regions consist of 10 repeated QD layers as indicated in the figures. Different QD growth conditions are used in the three batches.

We noticed that the surface treatment is of critical importance in the fabrication process of InAs-based mesa-etched devices. Mead and Spitzer reported that dangling bonds create states in the conduction band that causes Fermi-level pinning in an InAs/gold interface [128]. This also occurs in InAs/vacuum interfaces [129] and the approximate energy spacing to the conduction band edge was determined to 130 mV by Bhargava *et al.* [130].

The resulting effect is a surface inversion layer in the InAs/vacuum interface that can act as a conducting channel facilitating surface leakage currents in mesa-etched devices. The surface inversion layer is schematically indicated in Fig. 23.
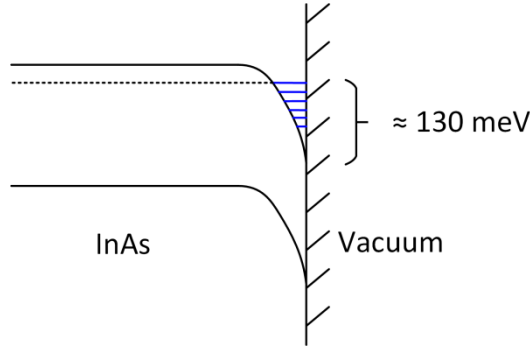
Figure 23. Surface inversion in the InAs/vacuum interface caused by Fermi level pinning.

A number of processing methods to reduce surface leakage in InAs diodes can be found in the literature [131, 132]. Marshall *et al.* reported that the etchant chemistry plays an important role [131]. Lin *et al.* also demonstrated that the addition of an intrinsic layer layer (0.72 μm) in InAs diodes can help reduce the leakage current [133, 134]. In this work we have used a process based on the work by Chaghi *et al.* [135]. It involves mesa-formation by wet-etching with a $H_3PO_4/H_2O_2/H_2O/C_6H_8O_7$ solution followed by a polishing etch with $C_6H_8O_7/H_2O_2$, heat treatment at 275 °C, a $NaClO/H_2O$ polishing etch and mesa encapsulation by photoresist. All steps were employed in the three batches except for the first batch which did not receive the $NaClO/H_2O$ polishing etch and the photoresist encapsulation. A more detailed description of the process can be found in the appendix.

A variety of features are defined in the mask-set used to fabricate the devices. Notably, it includes non-covered mesas for normal incidence photocurrent measurements with sizes in the range 30-1000 μm. In addition, metal-covered mesas are available for electrical measurements. Figure 24 shows a micrograph of a fabricated chip containing several single-pixel devices.
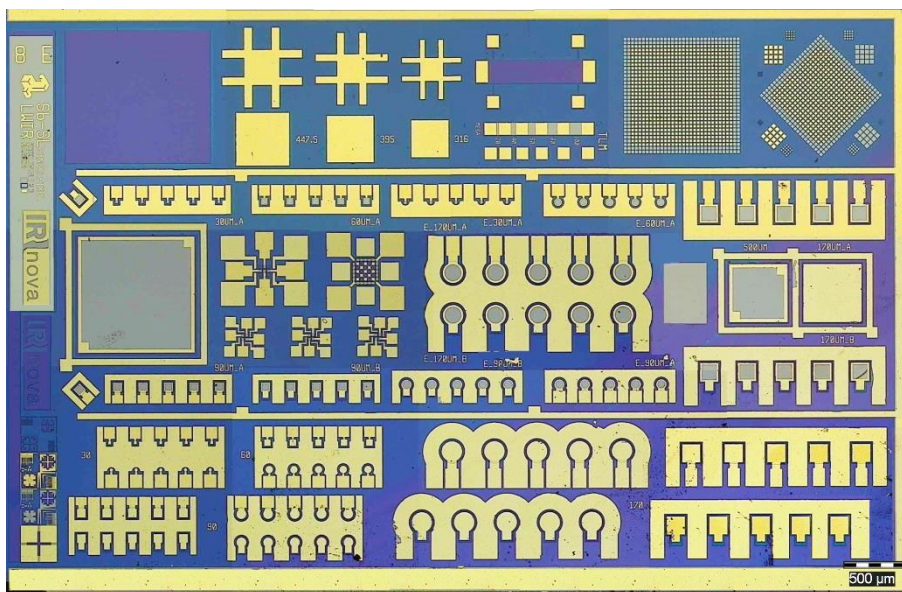
Figure 24. Micrograph of a chip containing single-pixel photodetectors with mesa sizes in the range 30-1000 µm.

A summary of the relevant parameters for the three device batches is presented in Tab. 2.

Batch	Measured peak PL wavelength (µm)	QD growth parameters	Process parameters	Intrinsic region thickness (µm)
A	4.1	InSb 3 ML, 490 °C, V/III=1.6	$H_3PO_4/H_2O_2/H_2O/C_6H_8O_7$ $C_6H_8O_7/H_2O_2$ Heat treatment	1.05
B	6.2	InSb 8 ML 470 °C, V/III=0.8	$H_3PO_4/H_2O_2/H_2O/C_6H_8O_7$ $C_6H_8O_7/H_2O_2$ Heat treatment NaClO/H_2O Encapsulation	1.7
C	6.5	$In_{0.5}Ga_{0.5}Sb$ 12 ML, 530 °C, V/III=1.2	$H_3PO_4/H_2O_2/H_2O/C_6H_8O_7$ $C_6H_8O_7/H_2O_2$ Heat treatment NaClO/H_2O Encapsulation	1.7

Table 2. Summary of the design parameters of batch A-C.

6.2 Device results

6.2.1 Batch A

Figure 25a shows the measured photoresponse and photoluminescence as a function of energy and wavelength in a single-pixel device from batch A. The photoresponse, indicated in blue, has a contribution from the InAs matrix with a cut-off close to 3 μm whereas the shoulder extending to approximately 5 μm originates from type-II transitions from bound QD states to continuum states in the matrix. The QD PL from the same device shows a peak at 4.1 μm, indicated in red. Figure 25b shows the dark current density measured in a 170 x 170 μm² device from batch A. The majority of the devices in batch A have non-rectifying I-V behavior and high dark currents. Current density measurements on different mesa sizes indicate that surface currents contribute to the dark current. The best devices show photoresponse up to 100 K.
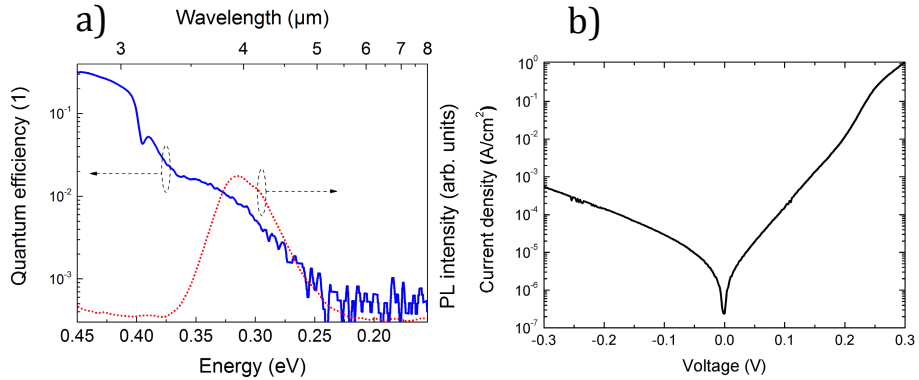
Figure 25. a) Photoresponse and photoluminescence measured in a 170 x 170 μm² device at 77 K. b) Dark current density at 77 K.

6.2.2 Batch B

The photoresponse at 77 K of a batch B device is shown as a function of energy and wavelength in Fig. 26a. In addition, the PL from a corresponding multilayer QD sample is shown in the same figure, indicated in red. The photoresponse, indicated in blue, extends up to 6 μm in accordance with the measured QD-related PL which peaks at 6.2 μm. The quantum efficiency is significantly lower than in batch A but increases up to 0.3 % at 5 μm and 140 K which is the highest temperature at which photoresponse can be measured in batch B devices. Figure 26b furthermore shows the dark current density as a function of applied bias in the temperature range 80-140 K. The dark current is significantly lower than in batch A, although the effective type-II bandgap is

smaller. This indicates that the additional process steps of NaClO/H_2O polishing etch and photoresist encapsulation is an improvement. The dark current activation energy at 0.05 V reverse bias, extracted from an Arrhenius plot of the data in Fig. 26b, is 0.12 eV.
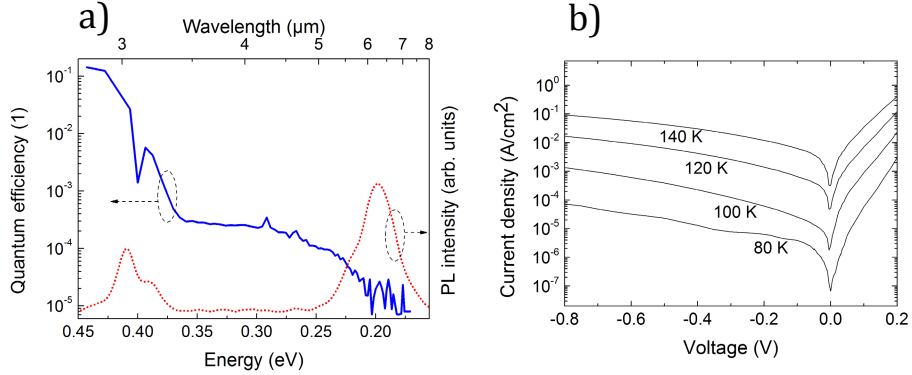
Figure 26. a) Photoresponse and photoluminescence measured in a 170 x 170 μm² device at 80 K. b) Dark current density at 80-140 K.

6.2.3 Batch C

Figure 27a shows the photoresponse of a 170 x 170 μm² batch C device as a function of energy and wavelength measured at 59-230 K. The PL from the same device structure measured at 77 K is shown in red with a QD-related peak at 6.5 μm. It was obtained after etching away the contact layer and the majority of the intrinsic layer. We note that the PL is shifted compared to the 10-QD-layer sample presented in Fig. 16a, which was grown with the same QD growth parameters. This suggests that the inclusion of the QDs in the thicker n-i-p structure has affected the QD growth as compared to the test structures in section 5.2.2. The photoresponse originating from type-II transitions is highly temperature-dependent with signal up to 8 μm for temperatures > 200 K. This was studied in detail in a large temperature range enabled by the lower dark current as compared to batch A and B. A detailed discussion on the temperature dependence is presented in Paper D.

Figure 27b shows the dark current density plotted as a function of applied bias in the temperature range 52-250 K. The measurement at 52 K is limited by photocurrent due to non-optimal cryostat shielding. At higher temperatures the dark current is thermally activated with an activation energy of 0.23 eV. Dark current density measurements on different mesa sizes indicate a smaller surface current contribution as compared to previous batches. In addition, the yield of low dark current devices is significantly improved with respect to batch A and B reaching 60% in the best chip which suggests an improvement

in the processing, or alternatively in the epitaxial quality of the detector material. The batch C devices have by far the lowest dark current of the series.
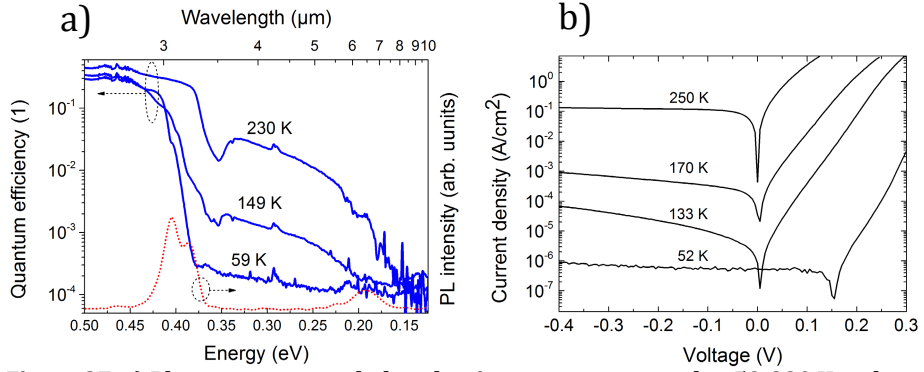
Figure 27. a) Photoresponse and photoluminescence measured at 59-230 K and 77 K respectively. b) Dark current density at 52-250 K.

6.3 Performance comparison

In the following we present a comparison of the D^* and NETD of the type-II interband $In_{0.5}Ga_{0.5}$ QD photodetectors from batch C (Sec. 6.2.3) and more established technologies.

6.3.1 D^*

D^* was calculated for an $In_{0.5}Ga_{0.5}Sb$ QD type-II photodetector with an f/2 aperture and a black body temperature of 300 K in the spectral range 3.5-8 μm, based on the measured quantum efficiency and dark current presented in Section 6.2.3 and Paper D. In Table 3 we compare the result with data from common detector types estimated by Martyniuk and Rogalski [136]. Only thermal noise and shot noise are taken into account in the type-II QD photodetector case.

	Quantum efficiency	BLIP temperature (λ_c=10 μm)	D^* (cmHz$^{1/2}$/W)
MCT	67 %	120 K	8×10^{11}(λ_c=10 μm,100 K)
QWIP	33 %	65 K	2×10^9 (λ_c=10 μm,100 K)
QDIP	2 %	120 K	2×10^{10} (λ_c=10 μm,100 K)
Type-II InGaSb QD photodetectors	0.01-0.05%	-	5×10^8 (λ_c=8 μm,136 K)

Table 3. Figure of merits for common detector types [136] compared to type-II InGaSb QD photodetectors at f/2 and a 300 K background. The incident radiant power is calculated in the 3.5-8 μm spectral range for the case of the type-II InGaSb QD photodetector.

6.3.2 Noise-equivalent temperature difference (NETD)

The NETD was calculated for a type-II interband $In_{0.5}Ga_{0.5}$ QD photodetector based on the results presented in Section 6.2.3 and in Paper D. The imaging conditions are the following: 30 °C scene temperature, f/4 aperture, ISC9705 ROIC and a 28 x 28 μm^2 pixel size. The integration time is defined by the time needed to fill the ROIC capacitor to 80 % for an 80 °C scene temperature. The noise types considered are thermal noise, ROIC noise and shot noise at a bandwidth of half the reciprocal integration time.

Table 4 lists some examples of NETD values for different detector types including the calculated value for the $In_{0.5}Ga_{0.5}Sb$ QD type-II photodetector.

Technology	Manufacturer	Architecture	Spectral range (µm)	Operating temperature (K)	Integration time (ms)	f/#	NETD (mK)
MCT	Sofradir [152]	384x288 25x25 µm²	7.7-9.5	77-80	3.5	f/2	17
MCT	Selex-ES [153]	640x512 24x24 µm²	8-10	up to 90			20
QWIP	IRnova [155]	640x480 25x25 µm²	7.5-9.0	-	< 33	f/2.7	15
QWIP	QmagiQ [32]	640x512 23x23 µm²	8.7 peak	68	5-10	f/4	25-30
QWIP	Sofradir [154]	640x512 20x20 µm²	8-9	73	7	f/2	31
Type-II InGaSb QD	-	-	3.5-8	136	96	f/4	628

Table 4. FPA performance of MCT and QWIP sensors. Calculated values of type-II In$_{0.5}$Ga$_{0.5}$Sb QD photodetectors are included in the comparison.

7 Type-II quantum-dot superlattice photodetectors

In the initial stages of this thesis photodetector designs based on QD superlattices were considered. The design idea relies on formation of QD stacks of alternating InAs and GaSb QDs grown in close proximity to each other so that minibands are formed with a bandgap corresponding to the LWIR spectral range. The matrix material is GaAs, which doesn't require surface passivation due to the deep level surface states [137] and has great manufacturability advantages compared to SLSs grown on GaSb substrates. Schematics of the device structure and the band structure are shown in Fig. 28.
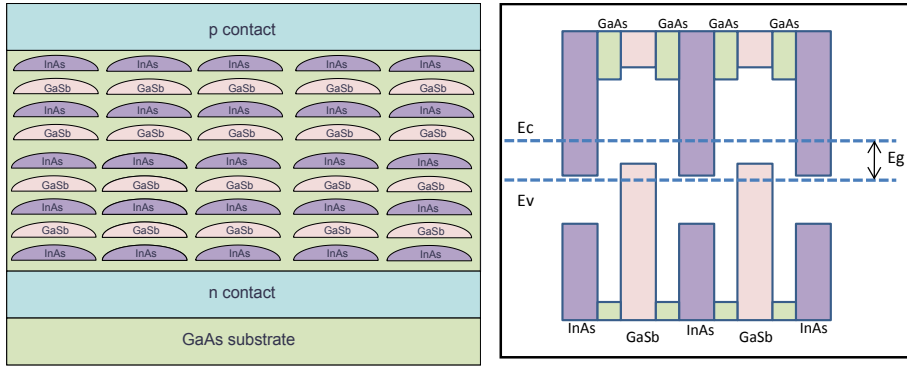
Figure 28. Schematic type-II QD superlattice photodetector device design and corresponding band structure. The bands are indicated in color whereas the bandgap is indicated in white. Reproduced from Ref. [138].

Hellström used an 8-band **k·p** model to calculate the electronic band structure and the absorption properties of type-II QD superlattice structures [139, 140]. An absorption coefficient of 1×10^4 cm^{-1} at 10 µm was calculated for lens-shaped InAs- and GaSb QDs with an assumed density of 1×10^{11} cm^{-2} separated by 2 nm GaAs in the growth direction [139]. The QD was assumed lens shaped with a diameter of 36 nm and a height of 7 nm and 6 nm for InAs and GaSb respectively. The single layer GaSb QD/GaAs structures that were grown in this work show a discrepancy of approximately 550 meV to the calculated hole energies in accordance with other published experimental results [PaperE] [141, 142, 143]. The well-known phenomena of antimony segregation and interdiffusion with the matrix are identified as the probable causes for the discrepancy [144, 145, 115]. Paper E investigates whether the GaAs lattice-matched In$_{0.49}$Ga$_{0.51}$P alloy can better serve as a matrix with less prominent effects of interdiffusion. In this study, we find that the discrepancy between theoretical and experimental values of the hole energy is reduced for GaSb QD

growth in an $In_{0.49}Ga_{0.51}P$ matrix. Nevertheless, the hole energy in the $In_{0.49}Ga_{0.51}P$ matrix is not in favor of realizing type-II QD superlattice photodetectors for the LWIR spectrum.

An alternative way of changing the conditions for Sb segregation with the matrix follows the idea of so-called "heterodots" by Ahopelto *et al.* [146]. Heterodots are coherently strained QDs on top of which another strained material is selectively deposited, presumably due to the strain conditions as argued by Ahopelto *et al.* [146], to form a heterojunction within the QD. Eyink *et al.* and Zhou *et al.* demonstrated InAs/GaSb heterodots grown on GaAs which they call heterojunction quantum dots or "HeQuaDs" [147, 148, 149, 150]. Zhou *et al.* furthermore demonstrated intra-QD type-II transition energies up to 1.56 µm [150]. This is the fundamental transition sought in the type-II QD superlattice design which is not likely to cover 10 µm even with interdiffusion-inhibiting tricks such as low-temperature growth and graded cap layers [58].

Besides the struggle for the correct transition energy, the type-II QD superlattice concept includes several engineering challenges such as promoting carrier transport once photoexcited electron-hole pairs are created, finding a suitable p-contact material and, perhaps most crucial, self-assembly of defect-free multiple-QD stacks coupled in the growth direction with a very small spacer layer in-between.

8 Conclusions and outlook

In summary, three variations of type-II interband QD photodetector structures were investigated: tensile strained (Al)GaAs(Sb) QD/InAs, compressively strained In(Ga)Sb QD/InAs and InAs/GaSb QD superlattices.

The design of InAs/GaSb QD superlattices grown on GaAs substrates [140] is attractive due to the properties of the GaAs matrix [112] which does not require passivation and has the potential for high manufacturability. One of the difficulties in realizing the concept, is to match the electron levels localized in the InAs QDs with the hole levels localized in the GaSb QDs so that the energy difference corresponds to the LWIR spectrum. Segregation and interdiffusion of Sb in GaSb QD growth acts to shift the energies to shorter wavelengths [117, 118, 91]. In Paper E we identify the $In_{0.49}Ga_{0.51}P$ alloy as an alternative matrix material that reduces the effects of Sb segregation and/or interdiffusion to an extent that is still not enough to allow for QD superlattice LWIR absorption. A second and maybe more crucial difficulty includes the engineering challenge of self-organizing the QD-superlattices uniformly and coherently over a full wafer, as would be required in FPA fabrication.

Tensile strained (Al)GaAs(Sb) QD/InAs bound-to-continuum photodetectors are considerably simpler in design, since no quantum mechanical coupling is required between the QD layers. Instead, infrared absorption occurs by photoexcitation from hole-states in the QDs to continuum-states in the matrix material. (Al)GaAs(Sb) QDs were grown by MOVPE and were characterized by microscopy, PL spectroscopy and absorption measurements. Transmission electron microscopy micrographs of 1.2 ML and 1.6 ML thick layers of GaAs deposited on InAs indicate that coherently strained QDs have formed. No QD-related photoluminescence could be measured in the (Al)GaAs(Sb) QD samples that were prepared. However, absorption measurements of samples with Si-doped QDs reveal absorption peaks in the range 5-12 μm. These peaks shift to longer wavelength for smaller nominal QD layer thicknesses and higher aluminium arsenide contents, as predicted for intraband absorption. Notably, no trend is seen for changes in the GaAsSb QD composition which could be explained by the simultaneous change in lattice constant and consequently the QD formation. Assuming that the observed absorption in the range 5-12 μm is intraband absorption, the interband transition can approximately be estimated from the difference of the InAs bandgap and the intraband transition, which

corresponds to the MWIR or LWIR spectrum. This makes (Al)GaAs(Sb) QDs an interesting material for infrared photodetector applications.

Much similar in design to (Al)GaAs(Sb) QD-based devices are In(Ga)Sb QD/InAs photodetectors which merely differ by the compressive strain and the type-III band alignment which covers the whole composition range [78]. In this thesis we have devoted a significant effort on extending the peak interband type-II transition wavelength, as measured by PL spectroscopy, in InSb QDs to record-long 6.2 μm [Paper C]. Growth of strain-reduced InGaSb QDs was explored and developed with PL up to 12 μm, owing to an increased QD size [Paper D]. During the course of the work, fabrication methods of mesa-etched p-i-n diodes were developed. This allowed for the demonstration of the first photovoltaic type-II interband QD photodetector in the MWIR, and later on devices with photoresponse just reaching the LWIR spectral range. There should also be good prospects of extending this well into the LWIR range, considering that PL was demonstrated up to 12 μm.

The photoresponse in type-II QD photodetectors is strongly temperature dependent which is attributed to hole trapping [Paper D]. The detector mechanism relies on thermal emission of the holes and temperatures approaching 200 K are needed for efficient extraction. At this temperature the dark current is too high for the devices to be useful. The viable alternative is to substitute the matrix material to one which provides less valence band confinement and facilitates the hole escape process. Paper D suggests $InAs_{1-x}Sb_x$ alloys which need to be grown metamorphically since no lattice-matched substrates are available for x > 0.09. Developing high-quality metamorphic $InAs_{1-x}Sb_x$ would most certainly be a significant undertaking which in addition most probably requires a re-optimization of the QD growth parameters due to the different lattice constant.

In the present type-II QD photodetector design the performance is limited by hole transport. The modeling of FPA performance, presented in Paper D, shows that the photocurrent is strictly smaller than the dark current at typical imaging conditions (f/4, 30 °C background). If the carrier transport issue can be overcome, type-II QD interband photodetectors have a potential to be highly interesting, mainly due to the dark current generation mechanism which is different than in MCT and QWIPs. If this is favorable, type-II QD interband photodetectors can possibly compete with QWIPs by an increased operating temperature.

References

[1] E. Barr, "Historical Survey of the Early Development of the Infrared Spectral Region," *Am. J. Phys.,* vol. 28, no. 42, pp. 42-54, 1960.

[2] P. Richards, "Bolometers for infrared and millimeter waves," *J. Appl. Phys.,* vol. 76, pp. 1-24, 1994.

[3] R. Watton, "Ferroelectric materials and devices in infrared detection and imaging," *Ferroelectrics,* vol. 91, pp. 87-108, 1989.

[4] W. T. Gray and D. I. Finch, "How accurately can temperature be measured?," *Phys. Today,* vol. 24, no. 9, pp. 32-40, 1971.

[5] A. Rogalski, "Comparison of photon and thermal detector performance," in *Handbook of Infrared Detection Technologies*, M. Henini and M. Razeghi, Eds., Guildford and King's Lynn, Elsevier Science Ltd., 2002, pp. 6-81.

[6] H. Dutton, Understanding Optical Communication, 1st ed., Research Triangle Park, NC, USA: IBM corporation, 1998.

[7] S. Martin and R. Miller, "Wireless multi-head smoke detector system". USA Patent 4160246, 3 07 1979.

[8] M. Jhabvala, D. Reuter, K. Choi, M. Sundaram, C. Jhabvala, A. La, A. Waczynski and J. Bundas, "The QWIP focal plane assembly for NASA's Landsat Data Continuity Mission," *Proc. SPIE,* vol. 7660, p. 76603J, 2010.

[9] M. Pirtini Cetingül and C. Herman, "Quantification of the thermal signature of a melanoma lesion," *International Journal of Thermal Sciences,* vol. 50, pp. 421-431, 2011.

[10] C. Connolly, "The use of infrared imaging in industry," *Assembly Automation,* vol. 25, no. 3, pp. 191-195, 2005.

[11] O. R. Dumitrescu, D. C. Baker, G. M. Foster and K. E. Evans, "Near infrared spectroscopy for in-line monitoring during injection moulding," *Polymer*

Testing, vol. 24, pp. 367-375, 2005.

[12] W. Boyle and G. Smith, "Charge coupled Semiconductor Devices," *Bell Sys. Tech. J.,* vol. 49, no. 4, pp. 587-593, 1970.

[13] J. Yon, E. Mottin, L. Biancardini, L. Letellier and J. Tissot, "Infrared Microbolometer Sensors and Their Applications in Automotive Safety," in *Advanced Microsystems for Automotive Applications*, Berlin Heidelberg, Springer, 2003, pp. 137-157.

[14] C. Vieider, S. Wissmar, P. Ericsson, U. Halldin, F. Niklaus, G. Stemme, J.-E. Källhammer, H. Pettersson, D. Eriksson, H. Jakobsen, T. Kvisteroy, J. Franks, J. VanNylen, H. Vercammen and A. VanHulsel, "Low-cost far infrared bolometer camera for automotive use," *Proc. SPIE,* vol. 6542, p. 65421L, 2007.

[15] F. Amon, N. Bryner and A. Hamins, "Evaluation of thermal imaging cameras used in fire fighting applications," *Proc. SPIE,* vol. 5407, pp. 44-53, 2004.

[16] M. Hinnrichs and N. Gupta, "Comparison of QWIP to HgCdTe detectors for gas imaging," *Proc. SPIE,* vol. 6940, p. 69401Q, 2008.

[17] W. Marinelli, C. Gittins, A. Gelb and B. Green, "Tunable Fabry-Perot etalon-based long-wavelength infrared imaging spectroradiometer," *Applied Optics,* vol. 38, no. 12, pp. 2594-2604, 1999.

[18] B. Cosofret, W. Marinelli, T. Ustun, C. Gittins, M. Boies, M. Hinds, D. Rossi, R. Coxe, S. Chang, B. Green and T. Nakamura, "Passive infrared imaging sensor for standoff detection of methane leaks," *Proc. SPIE,* vol. 5584, pp. 93-99, 2004.

[19] L. Yunting, W. Lingxue, L. Jiakun, Z. Changxing and Z. Bei, "Detectivity of Gas Leakage Based on Electromagnetic Radiation Transfer," *Proc. SPIE,* vol. 8013, p. 80130D, 2011.

[20] E. Naranjo, S. Baliga and P. Bernascolle, "IR Gas Imaging in an Industrial Setting," *Proc. SPIE,* vol. 7661, p. 76610K, 2010.

[21]   D. C. Dayton, J. Allen, R. Nolasco, J. D. Gonglewski, M. Myers, D. Burns, I. Mons and F. Maia, "Passive SWIR airglow illuminated imaging compared with NIR-visible for low light night time observations," *Proc. of SPIE,* vol. 8014, pp. 801407-1, 2011.

[22]   R. Serway, C. Moses and C. Moyer, in *Modern Physics*, 2nd ed., Brooks/Cole, Thomson learning, 1997, p. 69.

[23]   J. Miller, "Future sensor system needs for staring arrays," *Infrared Phys. Technol.,* vol. 54, pp. 164-169, 2011.

[24]   A. Rogalski, "Recent progress in infrared detector technologies," *Infrared Phys. Technol.,* pp. 136-154, 2011.

[25]   A. Rogalski, "Comparison of photon and thermal detectors performance," in *Handbook of Infrared Detection Technologies*, M. Henini and M. Razeghi, Eds., Guildford and King's Lynn, UK, Elsevier Science Ltd., 2002, p. 19.

[26]   H. Yan, M. Meixell, J. Zhang, P. Bey, J. Kimchi and L. Kilmer, "Low Dark Current Small Pixel Large Format InGaAs 2D Photodetector Array Development at Teledyne Judson Technologies," *Proc. of SPIE,* vol. 8353, pp. 838309-1, 2012.

[27]   I. Shtrichman, D. Aronov, M. ben Ezra, I. Barkai, E. Berkowitz, M. Brumer, R. Fraenkel, A. Glozman, S. Grossman, E. Jacobsohn, O. Klin, P. Klipstein, I. Lukomsky, L. Shkedy, N. Snapi, M. Yassen and E. Weiss, "High operating temperature epi-InSb and XBn-InAsSb photodetectors," *Proc. of SPIE,* vol. 8353, pp. 83532Y-1, 2012.

[28]   I. M. Baker, "HgCdTe 2D arrays-technology and performance limits," in *Handbook of Infrared Detection Technologies*, M. Henini and M. Razeghi, Eds., Guildford and King's Lynn, Elsevier Science Ltd., 2002, pp. 270-305.

[29]   M. Kinch, "HgCdTe: Recent Trends in the Ultimate IR Semiconductor," *J. Electron. Mat.,* vol. 39, no. 7, pp. 1043-1052, 2010.

[30]   W. Dyer and M. Tidrow, "Applications of MCT and QWIP to Ballistic Missile Defense," *Proc. SPIE,* vol. 3379, pp. 434-440, 1998.

[31]   B. Levine, "Quantumwell infrared photodetectors," *J. Appl. Phys.,* vol. 74, pp. R1-R61, 1993.

[32]   QmagiQ, "LWIR QWIP FPA "Hawk 512" datasheet," [Online]. Available: hhtp://www.qmagiq.com. [Accessed 24 03 2013].

[33]   M. Razeghi, H.-C. Lim, S. Tsao, M. Taguchi, W. Zhang and A. Quivy, "High performance mid-wavelength quantum dot infrared photodetectors for focal plane arrays," *Proc. SPIE,* vol. 6297, p. 62970C, 2006.

[34]   P. Martyniuk and A. Rogalski, "Quantum-dot infrared photodetectors: Status and outlook," *Progress in Quantum Electronics,* vol. 32, pp. 89-120, 2008.

[35]   A. Barve, J. Montoya, Y. Sharma, T. Rotter, J. Shao, W.-Y. Jang, S. Meesala, S. Lee and S. Krishna, "High temperature operation of quantum-dots-in-a-well infrared photodetectors," *Infrared Phys. Technol.,* vol. 54, pp. 215-219, 2011.

[36]   D. Smith and C. Mailhiot, "Proposal for strained type II superlattice infrared detectors," *J. Appl. Phys.,* vol. 6, no. 5, pp. 2545-2546, 1987.

[37]   C. Hill, J. Li, J. Mumolo and S. Gunapala, "MBE grown type-II MWIR and LWIR superlattice photodiodes," *Infrared Phys. Technol.,* vol. 50, pp. 187-190, 2007.

[38]   S. Bogdanov, B. Nguyen, A. Hoang and M. Razeghi, "Surface leakage current reduction in long wavelength infrared type-II InAs/GaSb superlattice photodiodes," *Appl. Phys. Lett.,* vol. 98, p. 183501, 2011.

[39]   N. Gautam, H. Kim, S. Myers, E. Plis, M. Kutty, M. Naydenkov, B. Klein, L. Dawson and S. Krishna, "Heterojunction bandgap engineered photodetector based on type-II InAs/GaSb superlattice for single color and bicolor infrared detection," *Infrared Phys. Technol.,* vol. 54, pp. 273-277, 2011.

[40]   E. Youngdale, J. Meyer, C. Hoffman, F. Baroli, C. Grein, P. Young, H. Ehrenreich, R. Miles and D. Chow, "Auger lifetime enhancement in InAs-Ga1-xInxSb superlattices," *Appl. Phys. Lett.,* vol. 64, pp. 3160-3162, 1994.

[41] H. Kim, O. Cellek, Z.-Y. Lin, Z.-Y. He, X.-H. Zhao, S. Liu, H. Li and Y.-H. Zhang, "Long-wave infrared nBn photodetectors based on InAs/InAsSb type-II superlattices," *Appl. Phys. Lett.,* vol. 101, p. 161114, 2012.

[42] Y. Jang, T. Badcock, D. Mowbray, M. Skolnick, J. Park, D. Lee, H. Liu, M. Steer and M. Hopkinson, "Carrier lifetimes in type-II InAs quantum dots capped with GaAsSb strain reducing layer," *Appl. Phys. Lett.,* vol. 92, p. 251905, 2008.

[43] K. Nishikawa, Y. Takeda, K. Yamanaka, T. Motohiro, D. Sato, J. Ota, N. Miyashita and Y. Okada, "Over 100 ns intrinsic radiative recombination lifetime in type II InAs/GaAs(1-x)Sbx quantum dots," *J. Appl. Phys,* vol. 111, p. 044325, 2012.

[44] Y. Jiang, M. Teich, W. Wang and J. Meyer, "Auger recombination in HgCdTe quantum wires and quantum boxes," *J. Appl. Phys,* vol. 71, pp. 3394-3396, 1992.

[45] J. Pan, "Reduction of the Auger rate in semiconductor quantum dots," *Phys. Rev. B,* vol. 46, no. 7, pp. 3977-3998, 1992.

[46] L.-W. Wang, M. Califano, A. Zunger and A. Franceschetti, "Pseudopotential Theory of Auger Processes in CdSe Quantum Dots," *Phys. Rev. Lett.,* vol. 91, no. 5, p. 056404, 2003.

[47] G. Zegrya and D. Samosvat, "Mechanisms of Auger Recombination in Semiconducting Quantum Dots," *Journal of Experimental and Theoretical Physics,* vol. 104, no. 6, pp. 951-965, 2007.

[48] J. Voelcker, "The Gunn Effect," *IEEE Spectrum,* vol. 26, no. 7, p. 24, 1989.

[49] H. Kroemer, "Quasi-electric fields and band offsets: Teaching electrons new tricks," *International Journal of Modern Physics B,* vol. 16, no. 5, pp. 677-697, 2002.

[50] Z. I. Alferov, "The double heterostructure: Concept and its applications in physics, electronics and technology," *International Journal of Modern Physics B,* vol. 16, no. 5, pp. 647-675, 2002.

[51] S. Dimitrijev, Principles of Semiconductor Devices, New York: Oxford University Press, Inc., 2006, pp. 383-385.

[52] S. Dimitrijev, Principles of Semiconductor Devices, New York: Oxford University Press, Inc., 2006, pp. 536-540.

[53] G. Stringfellow, Organometallic Vapor-Phase Epitaxy, San Diego: Academic Press, 1999, p. 3.

[54] C. Asplund, Doctoral thesis, Epitaxy of GaAs-based long-wavelength vertical cavity lasers, Kista, Sweden: KTH, 2003.

[55] G. Stringfellow, "Organometallic Vapor-Phase Epitaxy," 2nd ed., San Diego, Academic press, 1999, pp. 12-13.

[56] A. Aardvark, N. Mason and P. Walker, "The growth of antimonides by MOVPE," *Prog. Crystal Growth and Charact.,* vol. 35, no. 2-4, pp. 207-241, 1997.

[57] A. Semenov, O. Lyublinskaya, V. Solov'ev, B. Meltser and S. Ivanov, "Surface segregation of Sb atoms during molecular-beam epitaxy of InSb quantum dots in an InAs(Sb) matrix," *J. Cryst. Growth,* Vols. 301-302, pp. 58-61, 2007.

[58] J. He, F. Bao and J. Zhang, "Capping effect of GaAsSb and InGaAsSb on the structural and optical properties of type II GaSb/GaAs quantum dots," *Appl. Phys. Lett.,* vol. 100, p. 171914, 2012.

[59] J. Tersoff and F. LeGoues, "Competing Relaxation Mechanisms in Strained Layers," *Phys. Rev. Lett.,* vol. 72, no. 22, pp. 3570-3574, 1994.

[60] A. Woll, P. Rugheimer and M. Lagally, "Self-organized quantum dots," *International Journal of High Speed Electronics and Systems,* vol. 12, no. 1, pp. 45-78, 2002.

[61] T. Voronina, N. Zotova, S. Kizhayev, S. Molchanov and Y. Yakovlev, "Luminescence properties of InAs layers and p-n structures grown by metallorganic chemical vapor deposition," *Semiconductors,* vol. 33, no. 10, pp. 1062-1066, 1999.

[62] T. de Lyon, J. Woodall, M. Goorsky and P. Kirchner, "Lattice contraction due to carbon doping of GaAs grown by metalorganic molecular beam epitaxy," *Appl. Phys. Lett.,* vol. 56, pp. 1040-1042, 1990.

[63] G. Balakrishnan, J. Tatebayashi, A. Khoshakhlagh, S. Huang, A. Jallipalli, L. Dawson and D. Huffaker, "III/V ratio based selectivity between strained Stranski-Krastanov and strain-free GaSb quantum dots on GaAs," *Appl. Phys. Lett.,* vol. 89, p. 161104, 2006.

[64] S. Ohkouchi and N. Ikoma, "Shape Transition of GaAs Islands Grown on InAs (001) Surfaces," *Jpn. J. Appl. Phys.,* vol. 33, pp. L470-L472, 1994.

[65] V. Solovev, O. Lyublinskaya, A. Semenov, B. Meltser, D. Solnyshkov, Y. Terentev, L. Prokopova, A. Toropov, S. Ivanov and P. Kopev, "Room-temperature 3.9-4.3 μm photoluminescence from InSb submonolayers grown by molecular beam epitaxy in an InAs matrix," *Appl. Phys. Lett.,* vol. 86, p. 011109, 2005.

[66] D. L. Smith, in *Thin-film deposition: Principles and practice*, New York, USA, McGraw-Hill, Inc., 1995, p. 295.

[67] G. Bernatz, S. Nau, R. Rettig and W. Stolz, "Effect of MOVPE Growth Interruptions on the Gallium Arsenide Interior Interface Morphology," *Journal of Electronic Materials,* vol. 29, no. 1, pp. 129-133, 2000.

[68] See J.A. Venables, "Atomic processes in crystal growth," *Surface science,* Vols. 299-300, pp. 798-817, 1993, and references therein.

[69] J. Tersoff and D. R. Hamann, "Theory of the scanning tunneling microscope," *Phys. Rev. B,* vol. 31, no. 2, pp. 805-813, 1985.

[70] C. Ernerheim-Jokumsen and C. Reuterskiöld-Hedlund, Cross-Sectional Scanning Tunneling Microscopy Studies of In1-xGaxSb/InAs, Kista: Master thesis, KTH, Trita-ICT-EX 2012:169 , 2012.

[71] R. Timm, Formation, atomic structure, and electronic properties of GaSb quantum dots in GaAs, Doctoral Thesis, TU Berlin, 2007.

[72] B. Fain, J. Girard, D. Elvira, C. David, G. Beaudoin, A. Beveratos, I. Robert-

Philip, I. Sagnes and Z. Wang, "Electronic structure of cleaved InAsP/InP(001) quantum dots measured by scanning tunneling spectroscopy," *Appl. Phys. Lett.,* vol. 97, p. 171903, 2010.

[73] S. Gaan, G. He, R. Feenstra, J. Walker and E. Towe, "Electronic states of InAs/GaAs quantum dots by scanning tunneling spectroscopy," *Appl. Phys. Lett.,* vol. 97, p. 123110, 2010.

[74] Z. Ikonic, "Multiband envelope function (k.p) method," in *Quantum Wells, Wires and Dots*, 3rd ed., Chippenham, Wiltshire, UK, John Wiley and Sons Ltd., 2009, pp. 407-430.

[75] M. Cusack, P. R. Briddon and M. Jaros, "Electronic structure of InAs/GaAs self-assembled quantum dots," *Phys. Rev. B.,* vol. 54, pp. R2300-R2303, 1996.

[76] M. Grundmann, O. Stier and D. Bimberg, "InAs/GaAs pyramidal quantum dots: Strain distribution, optical phonons, and electronic structure," *Phys. Rev. B.,* vol. 52, pp. 11969-11981, 1995.

[77] M. Califano and P. Harrison, "Composition, volume, and aspect ratio dependence of the strain distribution, band lineups and electron effective masses in self-assembled pyramidal In1-xGaxAs/GaAs and SixGe1-x/Si quantum dots," *J. Appl. Phys.,* vol. 91, pp. 389-398, 2002.

[78] I. Vurgaftman, J. Meyer and L. Ram-Mohan, "Band parameters for III–V compound semiconductors and their alloys," *J. Appl. Phys.,* vol. 59, no. 10, pp. 5815-5875, 2001.

[79] V. Jovanovic, "Strained quantum wells," in *Quantum Wells, Wires and Dots*, 3rd ed., Chippenham, Wiltshire, UK, John Wiley and Sons, 2009, pp. 203-223.

[80] P. Kruse, "The photon detection process," in *Optical and Infrared Detectors*, R. Keyes, Ed., Berlin, Germany, Springer Berlin Heidelberg, 1980, pp. 5-69.

[81] A. Rogalski, "Comparison of photon and thermal detectors performance," in *Handbook of Infrared Detection Technologies*, M. Henini and M.

Razeghi, Eds., Guildford and King's Lynn, UK, Elsevier Science Ltd., 2002, p. 10.

[82]   A. Rogalski, "Comparison of photon and thermal detectors performance," in *Handbook of Infrared Detection Technologies*, M. Henini and M. Razeghi, Eds., Guildford and King's Lynn, UK, Elsevier Science Ltd., 2002, p. 17.

[83]   A. Rogalski, "Comparison of photon and thermal detectors performance," in *Handbook of Infrared Detection Tehnologies*, M. Henini and M. Razeghi, Eds., Guildford and King's Lynn, UK, Elsevier Science Ltd., 2002, p. 24.

[84]   I. M. Baker, "HgCdTe 2D arrays-technology and performance limits," in *Handbook of Infrared Detection Technologies*, M. Henini and M. Razeghi, Eds., Guildford and King's Lynn, Elsevier Advanced Technology, 2002, p. 293.

[85]   A. Rogalski, "Comparison of photon and thermal detectors performance," in *Handbook of Infrared Detection Tehnologies*, M. Henini and M. Razeghi, Eds., Guildford and King's Lynn, UK, Elsevier Science Ltd., 2002, pp. 24-25.

[86]   S. Ohkouchi, I. Tanaka and N. Ikoma, "Scanning Tunneling Microscopy of Initial Stages of GaAs Heteroepitaxy on Lattice-Mismatched Substrates," *Jpn. J. Appl. Phys.,* vol. 33, pp. 1489-1493, 1994.

[87]   S. Ohkouchi and N. Ikoma, "Role of Steps in GaAs Heteroepitaxial Growth on InAs(001) Surfaces," *Jpn. J. Appl. Phys.,* vol. 33, pp. 3710-3714, 1994.

[88]   D. Tenne, V. Haisler, A. Toropov, A. Bakarov, A. Gutakovsky, D. Zahn and A. Shebanin, "Raman study of self-assembled GaAs and AlAs islands embedded in InAs," *Phys. Rev. B,* vol. 61, no. 20, p. 13785, 2000.

[89]   A. Sitnikova, O. Lublinskaya, A. Toropov, O. Rykhova, S. Konnikov and S. Ivanov, "TEM study of GaAs/GaSb QD heterostructures," *Applied Surface Science,* vol. 234, pp. 28-32, 2004.

[90]   V. Solov'ev, A. Toropov, B. Meltser, Y. Terent'ev, R. Kyutt, A. Sitnikova, A. Semenov, S. Ivanov, Motlan, E. Goldys and P. Kop'ev, "GaAs in GaSb:

Strained Nanostructures for Mid-Infrared Optoelectronics," *Semiconductors,* vol. 36, no. 7, pp. 869-873, 2002.

[91] S. Lin and C. Lee, "Self-assembled GaAs antidots growth in InAs matrix on (1 0 0) InAs Substrate," *Physica E,* vol. 25, pp. 335-338, 2005.

[92] S. Ivanov, O. Lyublinskaya, A. Toropov, V. Solov'ev, A. Semenov, Y. Terent'ev, B. Meltser, A. Sitnikova, K. Thonke and R. Suaer, "MBE growth, photoluminescence and lasing properties of tensile-strained GaAs/GaSbAs QD nanostructures," *J. Cryst. Growth,* vol. 275, pp. e2321-e2326, 2005.

[93] C. Pryor and M.-E. Pistol, "Band-edge diagrams for strained III-V semiconductor quantum wells, wires, and dots," *Phys. Rev. B,* vol. 72, p. 205311, 2005.

[94] P. Harrison, "Solutions to Schrödinger's equation," in *Quantum Wells, Wires and Dots*, 3rd ed., Chippenham, Wiltshire, UK, John Wiley and Sons, Ltd, 2009, pp. 17-66.

[95] W. Wang, E. Mendez, T. Kuan and L. Esaki, "Crystal orientation dependence of silicon doping in molecular beam epitaxial AlGaAs/GaAs heterostructures," *Appl. Phys. Lett.,* vol. 47, no. 8, pp. 826-828, 1985.

[96] E. Tok, J. Neave, M. Fahy, F. Allegretti, J. Zhang, T. Jones and B. Joyce, "Influence of arsenic incorporation on surface morphology and Si doping in GaAs(110) homoepitaxy," *Microelectronics Journal,* vol. 28, pp. 833-839, 1997.

[97] A. Quivy, A. Sperandio, E. da Silva and J. Leite, "p-Type doping of GaAs(001) layers grown by MBE using silicon as a dopant," *J. Cryst. Growth,* vol. 206, pp. 171-176, 1999.

[98] E. Fitzgerald, "Dislocations in strained-layer epitaxy: theory, experiment, and applications," *Matrials Science Reports,* vol. 7, pp. 87-142, 1991.

[99] A. Norman, Mason, N.J, Fisher, M.J., J. Richardson, A. Krier, P. Walker and G. Booker, "Structural and optical characterisation of MOVPE self-assembled InSb quantum dots in InAs and GaSb matrices," *Inst. Phys.*

Conf. Ser., vol. 157, pp. 353-356, 1997.

[100] E. Glaser, B. Bennett, B. Shanabrook and R. Magno, "Photoluminescence studies of selfassembled InSb, GaSb, and AlSb quantum dot heterostructures," *Appl. Phys. Lett.,* vol. 68, pp. 3614-3616, 1996.

[101] S. Ivanov, A. Semenov, V. Solovev, O. Lyublinskaya, Y. Terentev, B. Meltser, L. Prokopova, A. Sitnikova, A. Usikova and A. Toropov, "Molecular beam epitaxy of type II InSb/InAs nanostructures with InSb sub-monolayers," *J. Cryst. Growth,* vol. 278, pp. 72-77, 2005.

[102] P. Carrington, V. Solov'ev, Q. Zhuang, A. Krier and S. Ivanov, "Room temperature midinfrared electroluminescence from InSb/InAs quantum dot light emitting diiodes," *Appl. Phys. Lett.,* vol. 93, p. 091101, 2008.

[103] P. Carrington, V. Solovev, Q. Zhuang, S. Ivanov and A. Krier, "InSb quantum dot LEDs grown by molecular beam epitaxy for mid-infrared applications," *Microel. J.,* vol. 40, pp. 469-472, 2009.

[104] O. Lyublinskaya, V. Solov'ev, A. Semenov, B. Meltser, Y. Terent'ev, L. Pokopova, A. Toropov, A. Sitnikova, O. Rykhova and S. Ivanov, "Temperature-dependent photluminescence from type-II InSb/InAs quantum dots," *J. Appl. Phys.,* vol. 99, p. 093517, 2006.

[105] J. Garcia, T. Mankad, P. Holtz, J. Wellman and P. Petroff, "Electronic states tuning of InAs self-assembled quantum dots," *Appl. Phys. Lett.,* vol. 72, no. 24, pp. 3172-3174, 1998.

[106] G. Lian, J. Yuan, L. Brown, G. Lim and D. Ritchie, "Modification of InAs quantum dot structure by the growth of the capping layer," *Appl. Phys. Lett.,* vol. 73, no. 1, pp. 49-51, 1998.

[107] B. Riel, K. Hinzer, S. Moisa, J. Fraser, P. Finnie, P. Piercy, S. Fafard and Z. Wasilewski, "InAs/GaAs(1 0 0) self-assembled quantum dots: arsenic pressure and capping effects," *J. Cryst. Growth,* vol. 236, pp. 145-154, 2002.

[108] F. Ferdos, S. Wang, Y. Wei, A. Larsson, M. Sadeghi and Q. Zhao, "Influence of a thin GaAs cap layer on structural and optical properties of InAs

quantum dots," *Appl. Phys. Lett.,* vol. 81, no. 7, pp. 1195-1197, 2002.

[109] Y. Chen and J. Washburn, "Structural Transition in Large-Lattice-Mismatch Heteroepitaxy," *Phys. Rev. Lett.,* vol. 77, no. 19, pp. 4046-4049, 1996.

[110] C. Larsen, S. Li and G. Stringfellow, "Decomposition Mechanisms of Trimethylantimony and Reactions with Trimethylindium," *Chem. Mater.,* vol. 3, pp. 39-44, 1991.

[111] A. Convertino, L. Cerri, G. Leo and S. Viticoli, "Growth interruption to tune the emission of InAs quantum dots embedded in InGaAs matrix in the long wavelength region," *J. Cryst. Growth,* vol. 261, pp. 458-465, 2004.

[112] F. Heinrichsdorff, A. Krost, M. Grundmann, D. Bimberg, F. Bertram, J. Christen, A. Kosogov and P. Werner, "Self organization phenomena of InGaAs/GaAs quantum dots grown by metalorganic chemical vapour deposition," *J. Cryst. Growth,* vol. 170, pp. 568-573, 1997.

[113] K. IIzuka, K. Mori and T. Suzuki, "Effects of growth interruption during the formation of InAs/GaAs self-assembled quantum dots grown by molecular beam epitaxy," *Microel. J.,* vol. 34, pp. 611-613, 2003.

[114] M. Hammar, F. LeGoues, J. Tersoff, M. Reuter and R. Tromp, "In situ ultrahigh vacuum transmission electron microscopy studies of hetero-epitaxial growth I. Si(001)/Ge," *Surface Science,* vol. 349, pp. 129-144, 1996.

[115] R. Timm, H. Eisele, A. Lenz, S. Becker, J. Grabowski, T.-Y. Kim, L. Müller-Kirsch, K. Pötschke, U. Pohl, D. Bimberg and M. Dähne, "Structure and intermixing of GaSb/GaAs quantum dots," *Appl. Phys. Lett.,* vol. 85, no. 24, pp. 5890-5892, 2004.

[116] D. Williams and C. Carter, "Weak-Beam Dark-Field Microscopy," in *Transmission Electron Microscopy - A Textbook for Materials Science*, New York, Springer, 2009, pp. 463-481.

[117] G. Abstreiter, P. Schittenhelm, C. Engel, E. Silveira, A. Zrenner, D.

Meertens and W. Jäger, "Growth and characterization of self-assembled Ge-rich islands on Si," *Semicond. Sci. Technol.,* vol. 11, pp. 1521-1528, 1996.

[118] A. Yakimov, A. Dvurechenskii, Y. Proskuryakov, A. Nikiforov, O. Pchelyakov, S. Teys and A. Gutakovskii, "Normal-incidence infrared photoconductivity in Si p-i-n diode with embedded Ge self-assembled quantum dots," *Appl. Phys. Lett.,* vol. 75, pp. 1413-1415, 1999.

[119] S. Tong, J. Liu, J. Wan and K. Wang, "Normal-incidence Ge quantum-dot photodetectorsat 1.5 μm based on Si substrate," *Appl. Phys. Lett.,* vol. 80, pp. 1189-1191, 2002.

[120] R. Laghumavarapu, A. Moscho, A. Khoshakhlagh, M. El-Emawy, L. Lester and D. Huffaker, "GaSb/GaAs type II quantum dot solar cells for enhanced infrared spectral response," *Appl. Phys. Lett.,* vol. 90, p. 173125, 2007.

[121] D. Alonso-Álvarez, B. Alén, J. García and J. Ripalda, "Optical investigation of type-II GaSb/GaAs self-assembled quantum dots," *Appl. Phys. Lett.,* vol. 91, p. 263103, 2007.

[122] C. Hill, A. Soibel, S. Keo, J. Mumolo, D. Ting and S. Gunapala, "Mid-infrared quantum dot barrier photodetectors with extended cutoff wavelengths," *Electron. Lett.,* vol. 46, no. 18, pp. 1286-1288, 2010.

[123] D. Ting, A. Soibel, C. Hill, S. Keo, J. Mumolo and S. Gunapala, "High operating temperature midwave quantum dot barrier infrared detector (QD-BIRD)," *Proc. SPIE,* vol. 8353, p. 835332, 2012.

[124] A. Rogalski, "New material systems for third generation infrared photodetectors," *Opto-Electron. Rev.,* vol. 16, no. 4, pp. 458-482, 2008.

[125] L. Botha, Shamba, P. and J. Botha, "Electrical characterization of InAs thin films," *Phys. Stat. Sol. (c),* vol. 5, no. 2, pp. 620-622, 2008.

[126] P. Chakrabarti, A. Gawarikar, V. Mehta and D. Garg, "Effect of Trap-assisted Tunneling (TAT) on the Performance of Homojunction Mid-Infrared Photodetectors based on InAsSb," *Journal of Microwaves and*

Optoelectronics, vol. 5, no. 1, pp. 1-14, 2006.

[127] M. Millea, M. McColl and A. Silver, "Electrical characterization of metal/InAs contacts," *Journal of Electronic Materials,* vol. 5, no. 3, pp. 321-340, 1976.

[128] C. Mead and W. Spitzer, "Fermi level position at semiconductor surfaces," *Phys. Rev. Lett.,* vol. 10, no. 11, pp. 471-472, 1963.

[129] H. Karlsson, G. Ghiaia and U. Karlsson, "Electron dynamics and accumulation on the InAs (110) surface," *Surface Science,* vol. 407, pp. L687-L692, 1998.

[130] S. Bhargava, H.-R. Blank, V. Narayanamurti and H. Kroemer, "Fermi-level pinning position of the Au-InAs interface determined using ballistic electron emission microscopy," *Appl. Phys. Lett.,* vol. 70, no. 6, pp. 759-761, 1997.

[131] A. Marshall, C. Tan, J. David, J. Ng and M. Hopkinson, "Fabrication of InAs Photodiodes with reduced surface leakage current," *Proc. SPIE,* vol. 6740, p. 67400H, 2007.

[132] R.-M. Lin, S.-F. Tang, S.-C. Lee, C.-H. Kuan, G.-S. Chen, T.-P. Sun and J.-C. Wu, "Room Temperature Unpassivated InAs p-i-n Photodetectors Grown by Molecular Beam Epitaxy," *IEEE Transactions on Electron Devices,* vol. 44, no. 2, pp. 209-213, 1997.

[133] R.-M. Lin, S.-F. Tang and C. H. Kuan, "Study of current leakage in InAs p-i-n photodetectors," *J. Vac. Sci. Technol. B,* vol. 18, pp. 2624-2626, 2000.

[134] R.-M. Lin, S.-F. Tang, S.-C. Lee and C.-H. Kuan, "Improvement of current leakage in the InAs photodetector by molecular beam epitaxy," *J. Cryst. Growth,* Vols. 227-228, pp. 167-171, 2001.

[135] R. Chaghi, C. Cervera, H. Aït-Kaci, O. Grech, J. Rodriguez and P. Christol, "Wet etching and chemical polishing of InAs/GaSb," *Semicond. Sci. Technol.,* vol. 24, p. 065010, 2009.

[136] P. Martyniuk and A. Rogalski, "Comparison of performance of quantum

dot and other types infrared photodetectors," *Proc. SPIE,* vol. 6940, p. 694004, 2008.

[137] W. Spicer, I. Lindau, P. Skeath and C. Y. Su, "Unified defect model and beyond," *J. Vac. Sci. Technol.,* vol. 17, pp. 1019-1027, 1980.

[138] H. Martijn, C. Asplund, H. Malm, S. Smuk, L. Höglund, O. Gustafsson, M. Hammar and S. Hellström, "Development of IR imaging at IRnova," *Proc. SPIE,* vol. 7298, p. 72980E, 2009.

[139] S. Hellström, Electronic Bandstructure and Optical Properties of InAs and GaSb Quantum Dot Superlattices, Stockholm: KTH Master thesis, 2008.

[140] J. Andersson, L. Höglund, B. Noharet, Q. Wang, P. Ericsson, S. Wissmar, C. Asplund, H. Malm, H. Martijn, M. Hammar, O. Gustafsson, S. Hellström, H. Radamson and P. O. Holtz, "Quantum structure based infrared detector research and development within Acreo's centre of excellence IMAGIC," *Infared Phys. Technol.,* vol. 53, no. 4, pp. 227-230, 2010.

[141] F. Hatami, N. N. Ledentsov, M. Grundmann, J. Böhrer, F. Heinrichsdorff, M. Beer, D. Bimberg, S. S. Ruvimov, P. Werner, J. Heydenreich, U. Richter, S. V. Ivanov, B. Y. Meltser, P. S. Kop'ev and Z. I. Alferov, "Radiative recombination in type-II GaSb/GaAs quantum dots," *Appl. Phys. Lett.,* vol. 67, no. 5, pp. 656-658, 1995.

[142] L. Müller-Kirsch, R. Heitz, U. W. Pohl, D. Bimberg, I. Häusler, H. Kirmse and W. Neumann, "Formation of GaSb/GaAs quantum dots in MOCVD growth," *Physica E,* vol. 13, pp. 1181-1184, 2002.

[143] M. Kudo, T. Mishima, S. Iwamoto, T. Nakaoka and Y. Arakawa, "Long-wavelength luminescence from GaSb quantum dots grown on GaAs substrates," *Physica E,* vol. 21, pp. 275-278, 2004.

[144] F. Hatami, M. Grundmann, N. N. Ledentsov, F. Heinrichsdorff, R. Heitz, J. Böhrer, D. Bimberg, S. S. Ruvimov, P. Werner, V. M. Ustinov, P. S. Kop'ev and Z. I. Alferov, "Carrier dynamics in type-II GaSb/GaAs quantum dots," *Phys. Rev. B.,* vol. 57, no. 8, pp. 4635-4641, 1998.

[145] O. Pitts, S. P. Watkins, C. X. Wang, V. Fink and K. L. Kavanagh, "Antimony segregation in GaAs-based multiple quantum well structures," *J. Cryst. Growth,* vol. 254, pp. 28-34, 2003.

[146] J. Ahopelto, H. Lipsanen, M. Sopanen, T. Koljonen and H. E.-M. Niemi, "Selective growth of InGaAs on nanoscale InP islands," *Appl. Phys. Lett.,* vol. 65, pp. 1662-1664, 1994.

[147] K. G. Eyink, D. H. Tomich, J. J. Pitz, L. Grazulis, K. Mahalingam and J. M. Shank, "Self-assembly of heterojunction quantum dots," *Appl. Phys. Lett.,* vol. 88, p. 163113, 2006.

[148] K. Eyink, D. H. Tomich, L. Grazulis, J. J. Pitz, K. Mahalingam, J. Shank, S. Munshi and B. Ulrich, "Self-assembly of heterojunction quantum dots(HeQuaDs)," *Proc. of SPIE,* vol. 6129, p. 61290B, 2006.

[149] K. Eyink, D. H. Tomich, S. Munshi, B. Ulrich, W. Rice, L. Grazulis, J. M. Shank and K. Mahalingam, "Photoluminescence Study of Self-Assembly of Heterojunction Quantum Dots(HeQuaDs)," *Proc. of SPIE,* vol. 6481, p. 648110O, 2007.

[150] Z. Zhou, Y. Xu, R. Hao, B. Tang, Z. Ren and Z. Niu, "Long-wavelength light emission from self-assembled heterojunction quantum dots," *J. Appl. Phys.,* vol. 103, p. 094315, 2008.

[151] Sofradir, "LWIR HgCdTe FPA "Venus LW" datasheet," [Online]. Available: www.sofradir.com. [Accessed 18 04 2013].

[152] Selex-ES, "Datasheet of "Eagle long wave infrared detector"," [Online]. Available: www.selex-es.com. [Accessed 18 04 2013].

[153] Sofradir, "Datasheet of "Sirius-LW 640x512 QWIP"," [Online]. Available: www.sofradir.com. [Accessed 18 04 2013].

[154] IRnova, "Product datasheet of "IRnova640 integral cooler DDCA"," 2013. [Online]. Available: www.ir-nova.se. [Accessed 30 04 2013].

Appendix

Main processing steps for single-pixel photodiodes

1. Mesa formation by wet-etching, H_3PO_4:citric acid:H_2O_2:H_2O 1:1:2:20

2. Mesa sidewall polishing-etch by citric acid: H_2O_2 5:1, 1 minute and then rinsing in DI H_2O for 1 minute

3. Top and bottom contacts, Ti=500 Å, Pt=500 Å, Au =2000 Å

4. Thermal treatment, 275°C, 5 minutes

5. Dip polishing using NaClO:H_2O 1:100, 10 s

6. Photoresist deposition

7. Photoresist curing, 200 ^{0}C, 2 hours

8. Chip cleaving

9. Chip-mounting on carrier

10. Wire bonding

The referred ratios are by volume. The H_3PO_4 solution contains 85 % H_3PO_4 by volume. The H_2O_2 solution contains 30 % H_2O_2 by volume. The citric acid solution contains a 1:1 ratio of citric acid monohydrate and H_2O by weight. The sodium hypochlorite solution contains 14 % active Cl^-.

Guide to the papers

Paper A: Long-wavelength infrared quantum-dot based interband photodetectors

Tensile-strained (Al)GaAs(Sb)/InAs QD structures are investigated for use as the absorber material in LWIR photon detectors. (Al)GaAs(Sb) QDs are grown with MOVPE and characterized using AFM, TEM and absorption measurements. Strong absorption is observed in the 6-12 μm spectral range. The wavelength-shifts observed for variations of QD layer thickness and composition indicate that the absorption originates in intra- valence band transitions. From this, the interband transition is estimated to the MWIR and LWIR spectral regions, which suggests that (Al)GaAs(Sb)/InAs QD structures can be suitable as an IR detector material.

Author contribution: Material growth and experiment planning, AFM characterization, part of the absorption measurements, calculations, data analysis, writing the paper

Paper B: Photoluminescence and photoresponse from InSb/InAs-based quantum dot structures

In(Ga)Sb/InAs QD structures are fabricated by MOVPE and characterized using PL spectroscopy, STM and photocurrent measurements. Photoluminescence is demonstrated with peak emission up to 8.5 μm. Photoresponse in a p-i-n photodiode is demonstrated up to 6 μm at 80 K. The results suggest that InSb-based QD structures have a potential as a photon detector material for the LWIR spectral range.

Author contribution: Material growth and experiment planning, part of the PL measurements, part of the photocurrent measurements, data analysis, writing the paper

Paper C: Long-wavelength infrared photoluminescence from InGaSb/InAs quantum dots

The influence of Ga in the growth of InGaSb QD/InAs structures is investigated. Peak photoluminescence is demonstrated beyond 8 μm at 77 K which is longer than what has been reported for InSb QDs. The results indicate that InGaSb

QDs can be grown at a larger size than InSb QDs which is interpreted to be an effect of the reduced strain.

Author contribution: Material growth and experiment planning, calculations, analysis, writing the paper

Paper D: A performance assessment of type-II interband In$_{0.5}$Ga$_{0.5}$Sb QD photodetectors

In$_{0.5}$Ga$_{0.5}$Sb/InAs QD photodiodes are demonstrated with photoresponse up to 8 μm at 230 K. A strong temperature dependence in the photoresponse is observed, which is attributed to hole trapping in the QDs. This limits the device performance at typical imaging temperatures (60-120 K). A replacement of the matrix material to an InAsSb alloy is proposed as a mean to facilitate the thermionic emission of holes and thereby enhance the photoresponse and detector performance.

Author contribution: Material growth, calculations, data analysis, writing the paper

Paper E: GaSb/Ga$_{0.51}$In$_{0.49}$P self assembled quantum dots grown by MOVPE

MOVPE is used to grow GaSb QDs in GaAs and Ga$_{0.51}$In$_{0.49}$P matrices. GaSb QD structures are studied with AFM, TEM and PL spectroscopy. The results show that the PL is in better correspondence with calculated values for GaSb QD/Ga$_{0.51}$In$_{0.49}$P structures as compared to GaSb QD/GaAs structures. This indicates that the effects of intermixing of GaSb QDs in a Ga$_{0.51}$In$_{0.49}$P matrix are reduced as compared to GaSb QDs grown in a GaAs matrix.

Author contribution: Material growth, AFM characterization, data analysis, writing the paper